FACULTAD DE CIENCIAS

VARIABILIDAD ESPACIO-TEMPORAL DE LA TURBIDEZ A PARTIR DE SENTINEL-2 EN EL SENO RELONAVÍ, PATAGONIA NORTE, CHILE.

Por

WIRMER GARCÍA TUÑON

TESIS PARA OPTAR AL

GRADO DE MAGÍSTER EN ECOLOGÍA MARINA

Director de Tesis: DR. CARLOS CRISTIAN LARA PEÑA

Co-Director de Tesis: DR. BERNARDO OSCAR BROITMAN ROJAS

DR. JESÚS VALERIANO DELEGIDO GÓMEZ

Concepción, Chile

2024

FACULTAD DE CIENCIAS

VARIABILIDAD ESPACIO-TEMPORAL DE LA TURBIDEZ A PARTIR DE SENTINEL-2 EN EL SENO RELONCAVÍ, PATAGONIA NORTE, CHILE.

Por

WIRMER GARCÍA TUÑON

Tesis para optar al grado de Magíster en Ecología Marina

El autor y el Director de Tesis certifican que la investigación presentada es original y cumple con las normas establecidas para todo aspecto relativo a su ejecución.

Concepción, Chile

2024

Universidad Católica de la Santísima Concepción

ACTA DE EXAMEN DE GRADO

En Concepción de Chile, a 22 de ABRIL de 2024 , vista y revisados los requisitos de Título/Grado presentados por:

Don **WIRMER . GARCÍA TUÑON**

RUT 26247151-9

Alumno de la Carrera de **MAGISTER EN ECOLOGIA MARINA**

Sede **CONCEPCIÓN** Jornada **DIURNO**

De la Universidad Católica de la Santísima Concepción, la Comisión Examinadora ha otorgado las siguientes calificaciones:

"VARIABILIDAD ESPACIOTEMPORAL DE LA TURBIDEZ A PARTIR DE SENTINEL-2 EN EL SENO RELONCAVÍ, PATAGONIA NORTE, CHILE."

Nombre	Calificación
JORGE LEON MUÑOZ **MIEMBRO INTERNO COMISIÓN DE TESIS**	**7,00 (SIETE)**
ESTHER URREGO DE MÁRQUEZ **MIEMBRO EXTERNO COMISIÓN DE TESIS**	**7,00 (SIETE)**
CARLOS LARA PEÑA **DIRECTOR DE TESIS**	
BERNARDO BROITMAN ROJAS **CO-DIRECTOR DE TESIS**	
MARIBET GAMBOA MENDEZ **MINISTRO DE FE**	
CALIFICACION FINAL DE EXAMEN	**7,00 (SIETE)**

SECRETARIO ACADÉMICO

DECANO

A mi madre, mi esposa y mi familia…..

AGRADECIMIENTOS

A mis compañeros de curso Tamara Huerta, Darío Navarrete y Franco Erazo, que desde el inicio nos apoyamos mutuamente, asimismo al resto de compañeros de Postgrados de la Universidad Católica de la Santísima Concepción, en especial Daniel González y Felipe Torres. Agradezco también el apoyo continuo e incondicional de mis profesores guías: Carlos Lara, Bernardo Broitman y Jesús Delegido. Además, a todos los académicos y administrativos de la Facultad de Ciencias de la UCSC que de una manera u otra formaron parte en mi desarrollo y formación como Máster en esta casa de estudios.

Mis más sinceros agradecimientos la Dirección del Programa de Magíster en Ecología Marina por haberme brindado la oportunidad de formar parte de la comunidad UCSC y a la Dirección de Postgrado UCSC por el financiamiento de mis estudios mediante la BECA interna de Postgrado. Al proyecto Fondo de Investigación Estratégica en Sequía - ANID FSEQ210030 y a su director Dr. Jorge León por hacerme partícipe en el mismo como becario. Además, al Laboratorio de Procesamiento de Imágenes de la Universidad de Valencia, destacando a Patricia Urrego por dedicar parte de su tiempo en colaborar y contribuir en este estudio.

A la Fundación Data Observatory (DO), Centro Tecnológico ANID No. DO210001 por hacerme participe y miembro becario de tan importante institución. En este sentido, quiero agradecer a todo el personal del DO, el equipo Operativo y el equipo Científico de Investigadores y Becarios, por su apoyo en la preparación y realización de este trabajo.

A todos mis amigos que de una forma u otra aportaron su granito de arena para que la etapa de Magíster fuera amena y productiva, destacando como pilares fundamentales de este proceso Lily, Luciana, Luciano Luis y Nicole.

Gracias a todas las personas que hicieron posible la obtención de este grado y contribuyeron en esta investigación.

TABLA DE CONTENIDOS

ÍNDICE DE TABLAS

ÍNDICE DE FIGURAS

RESUMEN

La turbidez es un parámetro clave para estimar la calidad del agua y la salud de los ecosistemas acuáticos. Desde hace décadas es un problema mundial que afecta negativamente a los ecosistemas acuáticos. La turbidez está asociada a la pérdida de transparencia del agua debido a la presencia de partículas, sedimentos, sólidos en suspensión y partículas disueltas en el agua, de origen natural o antropogénico. El objetivo de este estudio fue analizar la variabilidad espacio-temporal de la turbidez a partir de imágenes de Sentinel-2 (S2) en el fiordo y seno Reloncaví, Patagonia Norte, Chile. Descargamos 123 imágenes S2 de la Agencia Espacial Europea para ensamblar una serie temporal de 5 años (2016-2020) para cinco sitios de estudio (R1 a R5) ubicados a lo largo del eje hacia el mar desde el fiordo hacia el seno. Los resultados de las imágenes en color real y dos algoritmos Nechad (Nv09 y Nv16) señalaron una imagen del otoño austral de 2019 como la de mayor turbidez. Del mismo modo, tres imágenes del otoño austral de 2020 también presentaban valores de turbidez elevados. Las plumas de río turbias de mayor extensión se produjeron en el otoño de 2019 y 2020, correspondientes a las tormentas y eventos de escorrentía más severos del año y al valor de turbidez más alto. El algoritmo Nv16 mostró valores de turbidez ligeramente superiores a los resultantes del algoritmo Nv09. Las tendencias a lo largo de toda la serie temporal no fueron significativas en ninguno de los sitios de estudio. Sin embargo, las estimaciones de turbidez en los sitios R1 y R2 tendieron a aumentar con el tiempo, pero no en el resto de los sitios, donde la turbidez tendió a disminuir. El sitio R1 registró los valores más altos de turbidez, y los valores más bajos se registraron en R5. El mes de mayo se caracterizó por los valores más altos de turbidez. La aplicación de algoritmos a partir de imágenes de satélite de alta resolución demostró ser eficaz para la estimación y cartografía de este parámetro de calidad del agua en la zona de estudio.

Palabras claves: Turbidez, Teledetección, Propiedades Ópticas Inherentes y Aparentes, Color del Océano, Patrones Temporales, Monitore de Calidad de Agua.

ABSTRACT

Turbidity is a key parameter to estimate water quality and the health of aquatic ecosystems. For decades it has been a worldwide problem that negatively affects aquatic ecosystems. Turbidity is associated with the loss of water transparency due to the presence of particles, sediments, suspended solids and dissolved particles in the water, of natural or anthropogenic origin. The objective of this study was to analyze the spatio-temporal variability of turbidity from Sentinel-2 (S2) images in Reloncaví fjord and sound, Northern Patagonia, Chile. We downloaded 123 S2 images from the European Space Agency to assemble a 5-year time series (2016-2020) for five study sites (R1 to R5) located along the seaward axis from the fjord towards the sound. Results from Real Color Imagery and two Nechad algorithms (Nv09 and Nv16) singled an image from the austral autumn of 2019 as the one with the highest turbidity. Similarly, three images from the 2020 austral autumn also exhibited high turbidity values. The turbid plumes to the greatest extent occurred in the autumn of 2019 and 2020, corresponding to the most severe storms and runoff events of the year and the highest turbidity value. The Nv16 algorithm showed slightly higher turbidity values than those resulting from the Nv09 algorithm. Trends over the entire time series were not significant at any of the study sites. However, turbidity estimates at sites R1 and R2 tended to increase over time, but not at the rest of the sites, where turbidity tended to decrease. Site R1 recorded the highest turbidity values, and the lowest values were recorded at R5. The month of May was characterized by the highest turbidity values. The application of algorithms from high-resolution satellite images proved to be effective for the estimation and mapping of this water quality parameter in the study area.

Keywords: Turbidity, Remote Sensing, Inherent and Apparent Optical Properties, Ocean Color, Temporal Patterns, Water Quality Monitoring.

INTRODUCCIÓN

Turbidity stands out as a key parameter to understand the health of marine and aquatic ecosystems worldwide. Increases in turbidity are associated with the loss of water transparency due to the presence of suspended and/or dissolved material of natural or anthropogenic origin (Abirhire et al., 2020; Bilotta and Brazier, 2008; Grobbelaar, 2009; Smith, 2003). Visible light (400-700 nm) strongly declines with depth; hence turbidity compresses the euphotic depth and curtails the energy available for photosynthesis (Cloern, 1987; Davies-Colley and Smith, 2001; de Castro Medeiros et al., 2015; Kirk, 1985; Pérez-Ruzafa et al., 2019; Zohary et al., 2009). On the other hand, water-clouding components and substances may facilitate the dispersion of contaminants (Anderson et al., 2012; Díaz et al., 2019; Gelda et al., 2013; Quang et al., 2017; Soria et al., 2021; Vanhellemont and Ruddick, 2014). Coastal regions are of special concern; over a third of the global population inhabits the world's coastlines and depends on them for the provision of multiple ecosystem services, particularly in developing countries (Barragán and de Andrés, 2015). Turbidity in coastal marine and inner water systems can be influenced by algal blooms, suspended sediments, surface runoff, colored dissolved organic matter (CDOM), excessive nutrient inputs from agriculture or extreme rainfall events, among others (Abirhire et al., 2020; Babin et al., 2003; Brando et al., 2015; Lee et al., 2015; Mendes et al., 2014; Potes et al., 2012; Saldías et al., 2012). In this way, the scientific challenge of accurately and dynamically estimating turbidity and its causes is of major importance.

Methods to measure turbidity *in situ* include indirect metrics, such as the Secchi disk depth, or direct quantification using turbidimeters or nephelometers; these measurements are very accurate, but have limited spatial and temporal resolution and can be resource intensive (Alvado et al., 2021; Caballero et al., 2020; Delegido et al., 2019; Rodríguez-López et al., 2022; Sòria-Perpinyà et al., 2021; Zhan et al., 2022). Turbidity measurements are usually reported in Nephelometric Turbidity Units (NTU) and Formazin Nephelometric Units (FNU). A study by Anderson (2005) and Dogliotti et al. (2015) indicated that there is no difference between the units in which turbidity is expressed (NTU and FNU), and both turbidity units are comparable or equivalent units regardless of the instrument's technology used. To this end, ocean color remote sensing currently provides direct estimations of water turbidity and other environmental variables over multiple spatial and temporal scales (Aragonés et al., 2016; Caballero et al., 2019; Caballero and Stumpf, 2020; Khan et al., 2021). The widespread availability and access to satellite images, together with processed data from space missions and programs through web platforms (NASA, USGS, Copernicus,

among others) has exploded over the past decades (Duckey et al., 2006). Radiometers onboard earth observation satellites can measure light reflected from the planet surface in different wavelengths of the electromagnetic spectrum that can help us understand ecosystem dynamics (Claverie et al., 2018; Frantz, 2019). Multiple satellite missions now provide synoptic measurement of the properties and/or optical constituents of water such as CDOM, suspended solids (SS), among others (Aavaste et al., 2021; Kuhn et al., 2019; Sòria-Perpinyà et al., 2022; Vantrepotte et al., 2012; Werdell et al., 2018). Turbidity in water can be estimated through inherent and apparent optical properties (Inherent Optical Properties - IOPs and Apparent Optical Properties - AOPs, respectively), as well as through the Optically Active Constituents (OACs) that are present in aquatic ecosystems (Budhiman et al., 2012; Dogliotti et al., 2015; Kirk, 1984; Soriano-González et al., 2022).

Generally speaking, the presence and concentration of OACs are determined by factors that influence both, IOPs and AOPs of water. According to Morel and Prieur (1977) and Mobley (2001, 2022), IOPs are defined as the physical determinants of how light interacts with water and allow us to understand the absorption and scattering of electromagnetic radiation as a function of its various constituents. IOPs are independent of the light field (absorption and scattering coefficients) and their variations are directly related to changes in the concentration, size distribution and composition of OACs (Aavaste et al., 2021; Werdell et al., 2018). On the other hand, AOPs were defined by Preisendorfer (1976), Morel and Gentili (1993) and Mobley (2001) as the optical properties of water that are influenced by the distribution of the angles of incidence and the amount of light and illumination available in the environment, together with the concentration of substances present in the medium. That is, AOPs vary depending on how the medium is illuminated (i.e., radiance and reflectance) (Jerlov, 1957; Kirk, 1984; Mobley, 2001, 2022).

Empirical and semi-empirical algorithms from satellite imagery can be used to estimate water quality parameters such as total suspended solids (SS), CDOM, chlorophyll-a concentration (Chl-a) and turbidity in different ecosystems using the optical properties and OACs of water (e.g., Z. Lee et al., 2002; Nechad et al., 2009, 2010; Phuoc Hoang Son et al., 2013; Dogliotti et al., 2015; Balasubramanian et al., 2020; Magrì et al., 2023). In this way, the products derived from remote sensing allow the continuous monitoring of water quality in the ocean and coastal zone over time and the study of their association with different environmental drivers (Werdell et al., 2018). However, understanding the drivers of water quality and how they change under emergent anthropogenic threats requires an accurate assessment of the quality and bias of satellite estimates (Pahlevan et al., 2021; Sòria-Perpinyà et al., 2021; Vanhellemont, 2019; Vanhellemont and Ruddick, 2016, 2021).

Recently, high spatial and spectral resolution images from multispectral optical sensors such as Landsat OLI and Sentinel-2 (S2) have become a valuable tool to study the dynamics of water transparency (Khan et al., 2021; Kuhn et al., 2019; Rodríguez-López et al., 2022). The S2 mission of the Copernicus program has stood out for its reliability in studies and monitoring related to water quality parameters (Alvado et al., 2021; Caballero et al., 2020, 2018; Ciancia et al., 2020; Delegido et al., 2019; Pahlevan et al., 2017; Soomets et al., 2020; Sòria-Perpinyà et al., 2022, 2021; Zhan et al., 2022). The water of coastal zones, are generally optically complex, known as Case 2 waters (Jerlov, 1957; Mélin and Vantrepotte, 2015; Morel and Gentili, 1993; Morel and Prieur, 1977): turbidity is determined by the independent variation of OACs in the water (Aavaste et al., 2021; Babin et al., 2003; Odermatt et al., 2012; Uudeberg et al., 2020, 2019; Vantrepotte et al., 2012).

The Northern Patagonia (NP) coastal region (41-45°S) is characterized by a complex geomorphology and high spatiotemporal variability driven by natural and anthropogenic forcings (Curra-Sánchez et al., 2022; Iriarte et al., 2017; Lara et al., 2016, 2010; León-Muñoz et al., 2021; Saldías et al., 2019), which could be a proxy for the presence of turbidity in this ecosystem. Aquaculture of mytilids and salmonids, the main anthropic activity in the coastal areas of NP, has experienced enormous growth in recent years – Chile is among the top producers of mussels and salmons worldwide (FAO, 2022) – with the Reloncaví sound and fjord, at the equatorward edge of NP standing out for their intensive use (Astorga et al., 2018; Barria et al., 2012; Camelo-Guarín et al., 2021; Molinet et al., 2015, 2021).

This research seeks to understand the dynamics and drivers of water turbidity in the coastal zone of the Reloncaví area in Northern Patagonia following the major social, cultural and economic importance of this region, and inform future actions that promote the sustainable management of the coastal zone. To this end we take advantage of S2 imagery, emphasizing the importance of correcting the default algorithms in future studies assessing the spatio-temporal variability in coastal turbidity.

HIPÓTESIS

Hipótesis General

La turbidez en el seno Reloncaví varía temporal y espacialmente asociada al ciclo estacional de la precipitación y las descargas fluviales. La turbidez será mayor durante los meses de invierno en comparación con los meses de verano.

OBJETIVOS

Objetivo General

Analizar la variabilidad espacio-temporal de la turbidez a partir de imágenes satelitales Sentinel 2 en el Seno Reloncaví, Patagonia Norte.

Objetivos Específicos

- Validar los productos de turbidez resultante del algoritmo de Nechad (v2009 - Nv09 / v2016 - Nv16) en el software ACOLITE con datos de mediciones *in situ* de la boya oceanográfica en el seno Reloncaví, Patagonia Norte.
- Analizar la variabilidad espacial de la turbidez a partir de imágenes satelitales Sentinel 2 en el seno Reloncaví, Patagonia Norte.
- Analizar el comportamiento temporal de la turbidez a partir de imágenes satelitales Sentinel 2 en el seno Reloncaví, Patagonia Norte.

2. MATERIALES Y MÉTODOS

2.1. Study area

The Reloncaví sound located in Inner Sea Chiloé (ISC), Northern Patagonia, is a semi-enclosed basin of about 50 km in length (N-S) and a width of approximately 32 km (E-W), with depths that can reach 450 m. It is connected to the Pacific Ocean through the Chacao channel on the west (Figure 1, "GEBCO Gridded Bathymetry Data," n.d.; Pinilla Matamala, 2011; Valle-Levinson et al., 2007). The climate is temperate maritime with an annual rainfall between 3000 and 4000 mm per year, temperatures range between 7 and 10 °C in winter, and 12 and 15 °C in summer (Aguayo et al., 2019; Garreaud, 2018; Garreaud et al., 2013; Lara et al., 2018; Subiabre and Rojas, 1994). Weather can be highly variable, driving quick changes in sea surface temperature (SST) driven by strong southerly winds. Harmful algal blooms (HABs) are common (Díaz and Figueroa, 2023; Saldías et al., 2021; Sandoval et al., 2018; Soto-Mardones et al., 2009). Water circulation in the fjord and sound is influenced by tides, currents and winds (Pantoja et al., 2011; Pérez-Santos et al., 2021, 2019; Vásquez et al., 2021). The sound receives large freshwater discharges from the Reloncaví fjord, the drainage of the Puelo, Petrohué and Cochamó rivers. These andean rivers exhibit a pluvio-nival regime, resulting in large outflows of suspended and dissolved material into the coastal zone (Aguayo et al., 2019; Iriarte et al., 2014; León-Muñoz et al., 2013, 2021; Saldías et al., 2019). The Reloncaví fjord is one of the main areas for the capture of wild mussel seed (larvae), which are used locally for mussel aquaculture, in addition to the salmon farms located there (Barria et al., 2012; Buschmann et al., 2021, 2009; Camelo-Guarín et al., 2021; Molinet et al., 2021).

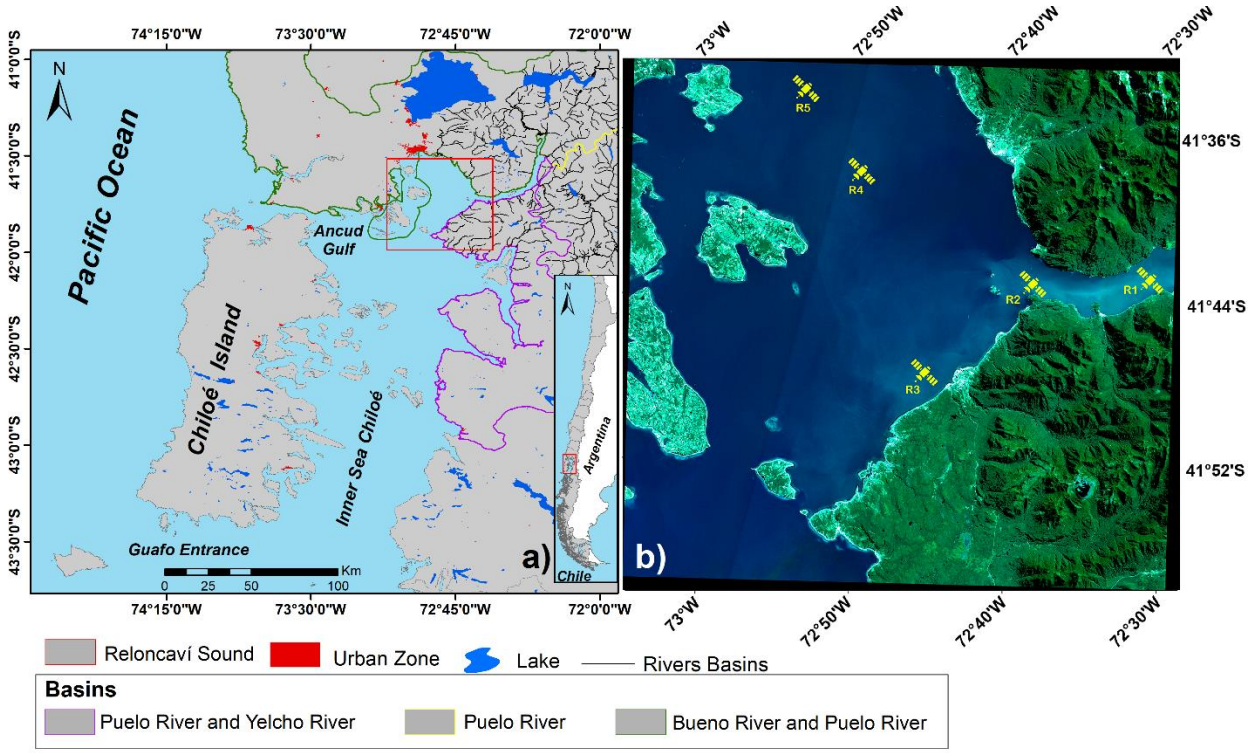

Figure 1. (a) Location of the study area in Northern Patagonia, the red rectangle indicates the Reloncaví Sound area, in red the urban area, in blue the lakes, in black lines the tributary rivers of the basins, the limits of the basins are represented in purple lines (Coastal between Puelo and Yelcho rivers), yellow (Puelo river) and green (basin and islands between Bueno and Puelo rivers). (b) True color image of the area enclosed in the red rectangle in (a) showing the spatial distribution of the sampling sites (R) in the Reloncaví Sound and fjord, which are distributed along the fjord (R1), fjord mouth (R2), fjord plume (R3), oceanographic buoy (R4) and away from the influence of riverine discharges (R5).

2.2. *In situ* turbidity, fluviometric and meteorological datasets

We used *in situ* turbidity data extracted for the period between November 2017 to July 2020 from a moored oceanographic buoy (OSIL's Fulmar) belonging to the i-mar Center of the Universidad de Los Lagos and Reloncaví Marine Observatory. The buoy is located in the Reloncaví sound at -41°38'10'' S and -72°50'4'' W, near site R4 (Figure 1b). Turbidity is measured using a multiparameter probe (AML Metrec XL). To store the turbidity dataset, the instrument has an hourly GSM transmission system and Campbell Scientific data logger. The extracted data were segmented to the mean of the values recorded between 14:00 and 15:00 hours, coinciding with the passover of the satellite in the study area, with a time difference window of ± 1 h. Turbidity data can be downloaded from the website http://www.cdom.cl/ (accessed May

2022). To study the spatial distribution of turbidity in the study area, five sites were selected (Figure 1b), located in the river (R1), river mouth (R2), river plume (R3), the point (R4) coincides with the location of the oceanographic buoy and a last point in the study area away from the influence of river discharges (R5). To illustrate the role of local meteorological forcing on turbidity, a time series of daily river flow and daily precipitation measured at the Puelo river meteorological station are presented. Precipitation and river flow data were downloaded from the Dirección General de Aguas (DGA, https://dga.mop.gob.cl/, accessed November 2023). The wind (speed and direction) values were taken from https://climatologia.meteochile.gob.cl/ in a three-day window (72 h) before the image acquisitions.

2.3. Remote sensing images and processing

The S2 mission consists of two twin satellites (2A/2B), which carry on board one MSI (Multispectral Instrument) sensor each, with a revisit frequency of 5 days (3 days for the study area). It is based on a constellation of two identical satellites in the same orbit, 180° out of phase with each other, and with a radiometric resolution of 12 bits. Table 1 shows the spectral and spatial resolution of S2 (ESA, 2015). The S2 scenes for the study area were free-downloaded from the Sentinel Science Data Center (https://scihub.copernicus.eu/dhus/#/home, accessed May 2022). These images were downloaded at Level 1C (L1C), which are radiometrically and geometrically corrected to the top of atmosphere (TOA). The Level-2A (L2A) product provides atmospherically corrected surface reflectance images, derived from the associated Level-1C products. The atmospheric correction (AC) of S2 images includes the correction of the scattering of air molecules (Rayleigh scattering), of the absorbing and scattering effects of atmospheric gasses, in particular ozone, oxygen and water vapor and the correction of absorption and scattering due to aerosol particles (ESA, 2015).

Table 1. Spectral and spatial resolution of S2.

Bands	Spectral region	Spatial resolution (m)	λ_{S2A} (nm)	λ_{S2B} (nm)	Bandwidth $_{S2A-S2B}$ (nm)
B1	Coastal aerosol	60	442.7	442.2	21 – 21
B2	Blue	10	492.4	492.1	66 – 66
B3	Green	10	559.8	559	36 – 36
B4	Red	10	664.6	664.9	31 – 31
B5	Red-edge1	20	704.1	703.8	15 – 16
B6	Red-edge2	20	740.5	739.1	15 – 15
B7	Red-edge3	20	782.8	779.7	20 – 20
B8	NIR	10	832.8	832.9	106 – 106

B8A	NIR narrow	20	864.7	864	21 -22
B9	Water vapor	60	945.1	943.2	20 – 21
B10	SWIR / Cirrus	60	1373.5	1376.9	31 – 30
B11	SWIR1	20	1613.7	1610.4	91 – 94
B12	SWIR2	20	2202.4	2185.7	175 - 185

We estimated turbidity from S2 image processing using ACOLITE (free software, https://github.com/acolite/), going from the L1C processing level to the L2A level. ACOLITE is a generic algorithm developed at Royal Belgian Institute of Natural Sciences (RBINS) for atmospheric correction and processing of satellite imagery for coastal and inland waters, allowing the correct estimation/validation of the turbidity parameter (Vanhellemont, 2019, 2020; Vanhellemont and Ruddick, 2018), supporting different types of multispectral and hyperspectral sensors, including S2 (Vanhellemont and Ruddick, 2016). We used the default DSF "Dark Spectrum Fitting" method for the software (Vanhellemont, 2019, 2020; Vanhellemont and Ruddick, 2018). All S2 images (L1C level) were atmospherically corrected with ACOLITE (version 20221114) and correspond to water reflectance at wavelength (λ), $\rho_w(\lambda)$, resampled to a pixel size of 10 m. $\rho_w(\lambda)$ is defined in equation 1:

$$\rho_w(\lambda) = \pi L_w(\lambda) / E_d^{0+}(\lambda) \quad (1)$$

where $L_w(\lambda)$ water-leaving radiance (after removal of air-water interface reflection) and $E_d^{0+}(\lambda)$ is the downwelling irradiance.

In addition, a built-in algorithm in ACOLITE optionally performs sunglint contamination corrections on SWIR band sensors (Harmel et al., 2018; Vanhellemont, 2019). We selected this sunglint correction to obtain the reflectance of the glint-free surface. Considering that most of the year our study area remains under the influence of clouds, we conducted a detailed visual inspection of each of the images in the date range of our study. The image selection process yielded a dataset with a maximum cloud cover (CC) of 57.9% for the full scene and a total of 123 images (see Table 2). Further details, such as image ID and CC are -provided in Supplementary Material 2 (SM 2).

Table 2. Number of selected Sentinel-2 images for the 2016-2020 period.

Month / Year	2016	2017	2018	2019	2020	Total
January	1	1	3	2	6	13
February	1	1	3	3	2	10
March	0	2	2	5	2	11
April	0	2	3	1	2	8
May	0	1	2	2	4	9
June	1	0	2	3	1	7

July	2	2	2	0	2	8
August	0	1	2	0	3	6
September	1	2	1	3	2	9
October	1	2	2	5	5	15
November	1	1	4	3	2	11
December	3	2	4	3	4	16
Total	11	17	30	30	35	123
0: No images available or No clear.						

2.4. Turbidity algorithms

ACOLITE incorporates two functions to estimate turbidity based on Nechad's algorithms (Nechad et al., 2009), hence we used both to estimate turbidity for all sites and dates (2009, Nv09, and 2016, Nv16, respectively). In Nechad's approach, turbidity is derived using a semi-empirical algorithm relating spectral reflectance to IOPs absorption and backscatter:

$$\text{Turbidity} = \frac{A_T\,\rho_w(\lambda)}{1-\rho_w(\lambda)/\mathrm{C}} + B_T \qquad (2)$$

where A_T, B_T and C are wavelength-dependent calibration coefficients that encompass IOPs characteristics (for more details see Nechad et al., 2009, 2010). Our study utilizes the red band (λ = 665 nm) implementation, with B4 related to S2 bands.

The oceanographic buoy located at R4 site provides *in situ* turbidity data in NTU units, yet for practical purposes we utilized in this study FNU units will be used for comparison with turbidity from Nechad's algorithms (Anderson, 2005; Dogliotti et al., 2015). The mean turbidity value was extracted in a 3x3 pixel kernel centered on the *in situ* measurement location, which we used to construct a time series for the 2016-2020 period.

2.5. Statistical analysis

Firstly, we carried out an exploratory analysis with all the *in situ* (buoy) turbidity data to detect outliers using descriptive statistics. After parsing outliers, *in situ* data were match-up with the data from the images available for the turbidity product. A total of 39 S2 satellite images were used for the match-up exercise of the R4 site and we examined the standard deviation (SD) in the 3x3 pixels spatial window to avoid possible outliers in the data. Then, we compared *in situ* turbidity and the Nv09 and Nv16 algorithms using linear regression and quantified the agreement using the coefficient of determination (R^2), Pearson's correlation (Pearson's r), root-mean-square-error (RMSE), centered root-mean-square-

error (CRMSE) difference, and the amplitude of their variations represented by their SD, which were visualized using a Taylor's diagram (Taylor, 2001). To compile the time series for each site we included the 123 images and used an exponential smoothing using the exponential window function from the Simple Time Series Analysis package from OriginPro 2023b 10.0.5.157 (Academic) software. We used a Mann-Kendall (MK) analysis to evaluate turbidity trends in each of the selected sites from R1 to R5. Finally, we analyzed a time series of records of precipitation and river flow data together with the turbidity values derived from the Nv09 algorithm at R1, the more landward station, to examine the role of environmental forcing on turbidity in the Reloncaví coastal ecosystem.

3. RESULTADOS

3.1. *In situ* turbidity data

Table 3 shows the statistics for *in situ* turbidity records during the 2017-2020 period. The turbidity values ranged from 0.18 FNU to 7.57 FNU across the year. The minimum value was recorded during austral spring (0.18 FNU), while the maximum was found in austral autumn. The overall mean of the 39 match-up values for *in situ* comparisons was 1.94 FNU.

Table 3. Descriptive statistics of *in situ* turbidity measured during the period 2017-2020.

Statistical / Season	Summer	Autumn	Winter	Spring	Annual
min (FNU)	0.31	2.05	0.5	0.18	0.18
max (FNU)	5.04	7.57	3.48	2.75	7.57
mean (FNU)	1.89	4.3	1.68	1.08	1.94
SD	1.59	2.08	1.09	0.87	1.72
CV (%)	84.04	48.34	64.87	80.87	88.84
n	14	6	5	14	39

min/max— minimum/maximum turbidity values, SD—standard deviation, CV—coefficient of variation and n—data number

3.2. Turbidity algorithms

Figure 2a shows the relation between the two algorithms (Nv09 and Nv16) and the *in situ* turbidity measurements (site R4). The linear relationship with *in situ* data for both algorithm's was nearly identical (R^2 = 0.40, Pearson´s r = 0.63, Fig. 2a). However, the Nv09 algorithm presented a lower RMSE than the Nv16 algorithm (see Figure 2a). A similar result was observed in the Taylor analysis (Figure 2b). The Nv09 and Nv16 algorithms reported a Pearson´s r = 0.63 (matching with the linear fit), and Nv09 presented lower variability among its data (SD = 0.83 FNU), with CRMSE less than 1.34 FNU. Therefore, it is possible to suggest that both algorithms have good correlation with *in situ* turbidity, although the Nv09 algorithm would be more reliable for developing a predictor model of turbidity due to lower CRMSE and SD.

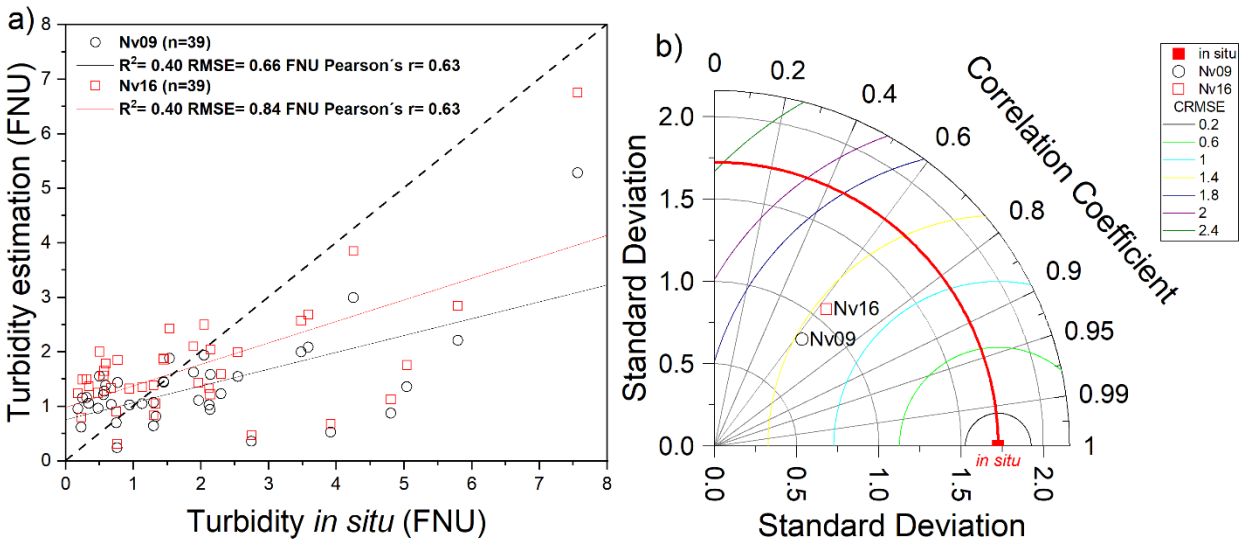

Figure 2. (a) Scatter plot between measured turbidity and the algorithms under study. The black circle and line represent the values from the Nechad 2009 algorithm (Nv09), while the red square and line are those resulting from the Nechad 2016 algorithm (Nv16). (b) Taylor diagram displaying a simultaneous statistical comparison of both algorithms and *in situ* measurement of turbidity. The colored contours indicate the CRMSE values.

Figure 3 shows true color (RGB) images derived from S2 images (top panel) and turbidity maps from Nv09 algorithm (bottom panel) for austral autumn. It was evident that the algorithm was capable of estimating lower and higher turbidity levels. The turbidity maps are presented in logarithmic scale following the high turbidity level observed during autumn. Using the Nv09 algorithm the highest estimated value was greater than $\log_{10}$ 1.29 FNU (19 FNU) for 2019/05/06 and 2020/05/20. It is important to note that the highest turbidity values observed in austral autumn correspond to large freshwater outflows from the Puelo river.

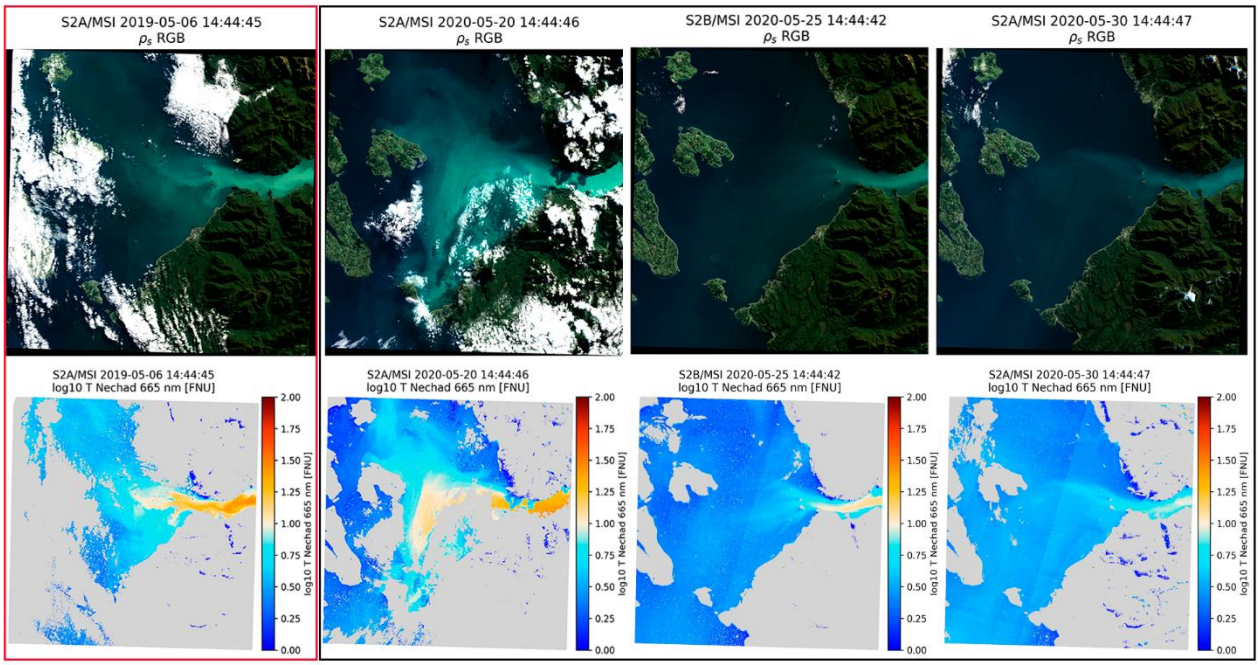

Figure 3. The top panels show true color (RGB) images and the bottom panels show results from the Nv09 algorithm for autumn days. The red panels show the image from the date with the highest turbidity on 2019/05/06. The black panels show the images from 2020/05/20, 2020/05/25 and 2020/05/30.

3.3. *Spatio-temporal analysis*

The use of both algorithms in all sites captured the same temporal pattern when estimating high and low turbidity values at all sites (see SM1 Figure 1, 2, 3) and hereafter we present values for the Nv09 algorithm. More information on the estimated turbidity values by both algorithms can be obtained from SM1.

During the austral summer, the values ranged from 0.3 FNU to 5 FNU, with R5 and R1 sites recording the lowest and highest values, respectively (see Figure 4, SM1 Figure 4). Turbidity was not very variable among all study sites with CV between 24% and 37%, sites R1 to R4 had a variation of less than 30%, only site R5 exceeded this figure (see SM1 Table 3, Figure 5a). It can be seen that, in space, stations closer to the river show higher turbidity values, while in time the highest values are observed during autumn and the lowest in spring (see Figure 4). Figure 5 shows that the lowest turbidity value was 0.090 FNU at site R5 (see SM1 Table 2). The austral springs were characterized by the lowest turbidity values, minimum values less than 1 FNU were detected at sites R3 to R5 (see Figure 4, 5). The highest turbidity values at this time

of year were obtained at sites R1 and R2, both exceeding 7 FNU and 4 FNU, respectively (see SM1 Figure 5d). These same sites showed low turbidity variability with respect to site R5, where CVs ranged from 31% to 57% during this season (see SM1 Table 6). On the contrary, the high turbidity values were found in the autumn season, specifically for the month of May (see Figure 4, SM1 Figure 4). Over the time series, the highest estimated turbidity value was 27.962 FNU in the austral autumn of 2019 at site R1 (see Figure 4, 5, SM1 Table 2). In this same season, one year later, high turbidity values were observed in all sites (see Figure 4). In that austral autumn of 2020, sites R2, R3 and R4 reached their maximum turbidity with values 19.556 FNU, 8.721 FNU and 5.285 FNU respectively (see Figure 3, SM1 Figure 5b). The highest turbidity variations were observed at site R1 and R2 in the austral autumn, while the lowest were observed at site R5 (see SM1 Table 4). Little variation in turbidity among all study sites was recorded in the austral winter with CVs ranging between 24% and 35%, similar to the behavior found in the austral summer, maximum values remained between 3 FNU and 4 FNU for all study sites (see Figure 5, SM1 Figure 5c). Although the highest variation was recorded at site R5 and the lowest at site R2, unlike what occurred in austral autumn (see SM1 Table 5). We observed no significant temporal trends in all the reconstructed time series. Although exponential smoothing and the MK test showed a slight increase in turbidity at sites R1 and R2 during the study period, this was not observed at sites R3, R4, and R5 (see Figure 5, SM1 Table 1).

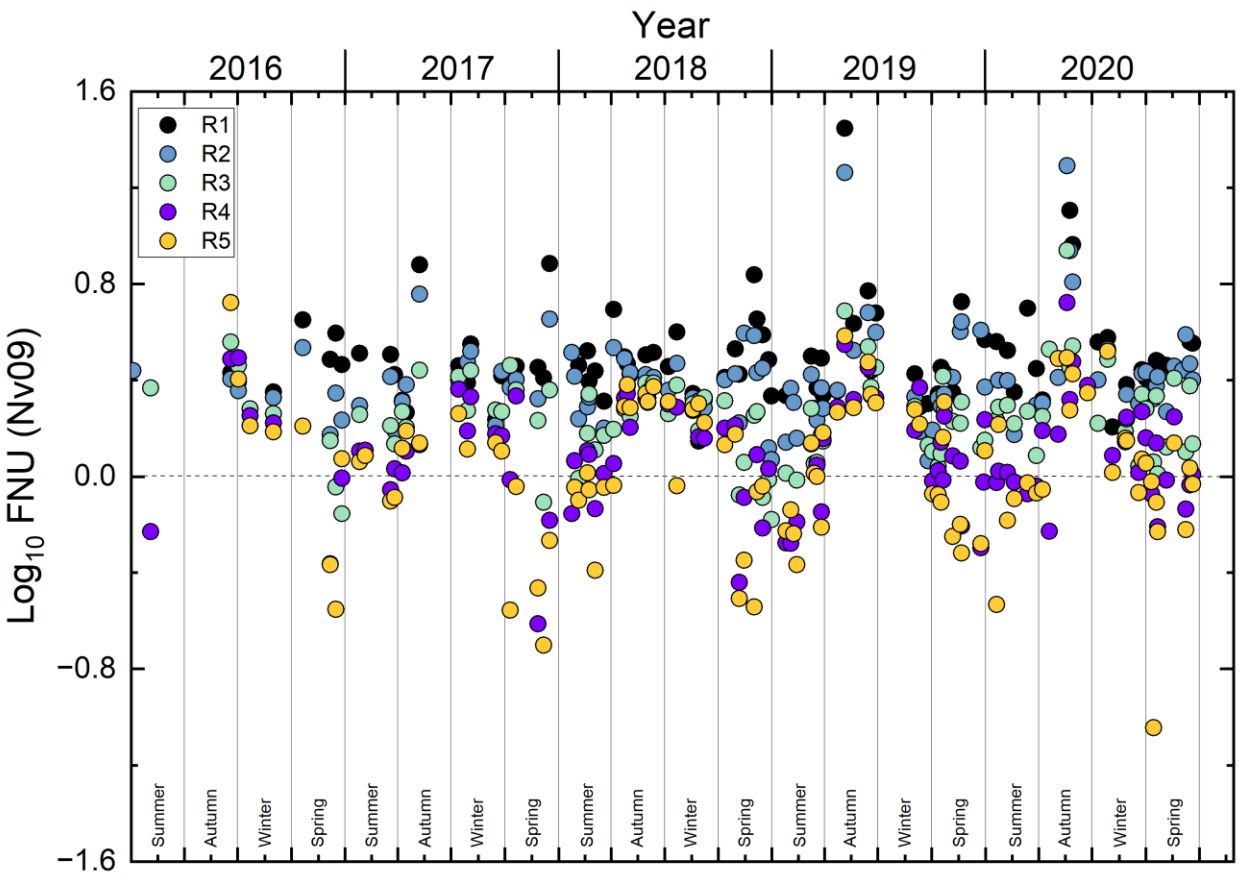

Figure 4. Spatio-temporal distribution of turbidity in log base derived from the Nechad 2009 algorithm (Nv09) for all sites, R1 in black, R2 in light blue, R3 mint, R4 purple and R5 mustard.

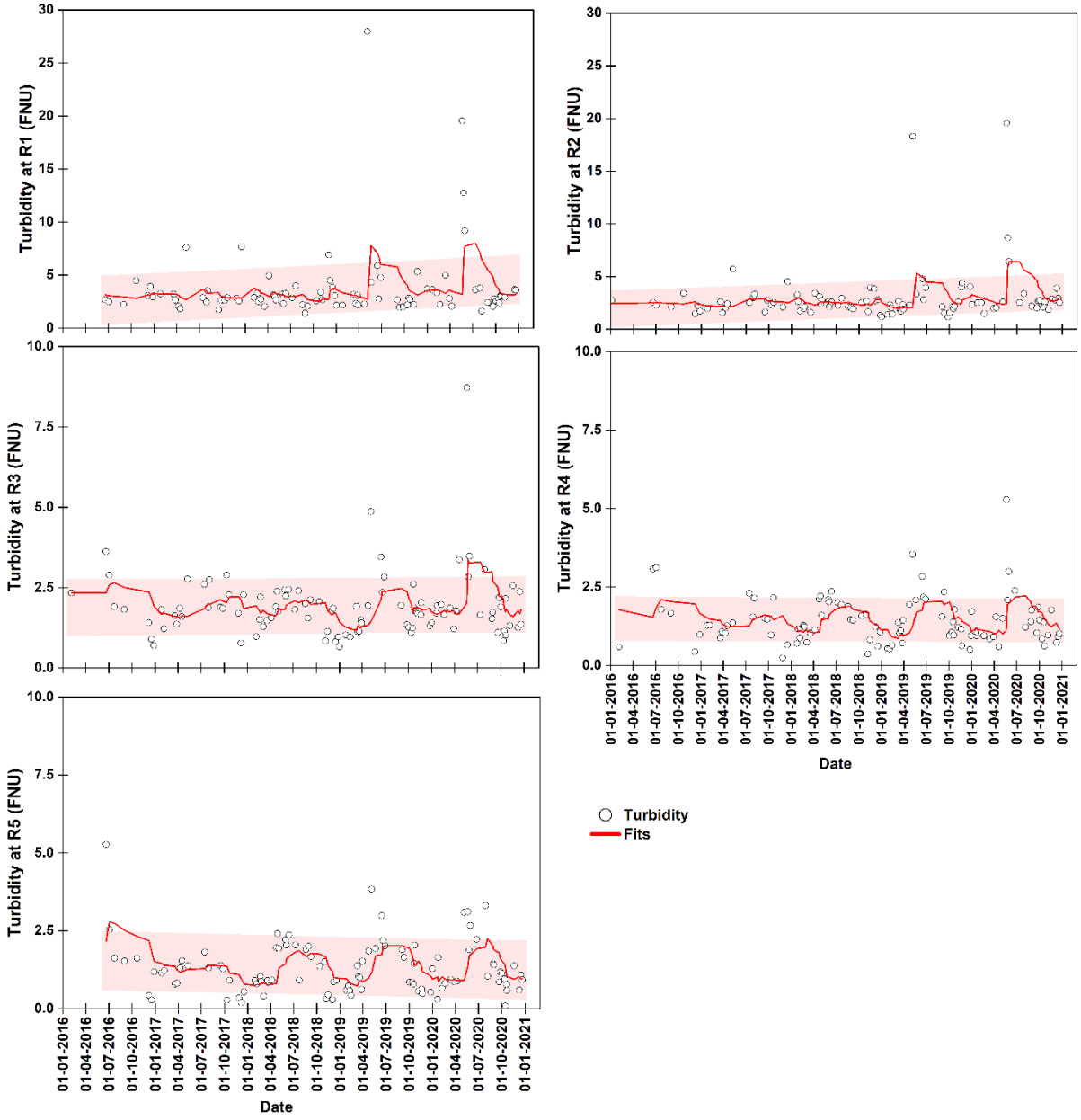

Figure 5. Turbidity time series constructed for all sites for 2016-2020 period. Black circles show the estimated turbidity times series from Nv09 algorithm, the red line represents the smoothing fit with prediction band 95% (confidence interval).

4. DISCUSIÓN

Worldwide, turbidity has been estimated for aquatic ecosystems through remote sensing using spectral band ratios and algorithms. The Nechad algorithms have been applied to multiple inland and coastal ecosystems around the world due to their accuracy in deriving high and low turbidity values. This was demonstrated by the studies of Nechad et al. (2009, 2010), Dogliotti et al. (2015), Novoa et al. (2017) and Tavora et al. (2023a). Particularly in Chile, the use of satellite algorithms has been influential in the estimation of the photosynthetically active light attenuation coefficient in an oligotrophic lake (Rodríguez-López et al., 2022). But studies related with spatial and temporal turbidity variability on marine ecosystems are still scarce.

Advances in algorithms for atmospheric correction (ACs) have allowed the accurate retrieval of bioptic parameters, among the turbidity in various aquatic ecosystems. Other studies (Table 4) have also detected turbid waters using other ACs (e.g., Delegido et al., 2019; Elhag et al., 2019; Sun et al., 2021; Zhan et al., 2022, Chowdhury et al., 2023).

Table 4. Studies that have estimated water turbidity, the atmospheric correction (AC) used, determination coefficients (R^2), correlation coefficients (r), root mean square error (RMSE), the aquatic ecosystem and location of each study.

Authors	AC	R^2	RMSE	Aquatic Ecosystem	Location
Delegido et al. (2019)	C2RCC, C2X and Polymer	0.34 - 0.82	1.4 NTU and 2.7 NTU	Reservoirs	Valencian community, Spain
Elhag et al. (2019)	Sen2Cor*	0.74 - 0.94	0.07 - 1.15 (NDTI)	Baysh Dam	Wadi Baysh, Saudi Arabia
Sun et al. (2021)	Acolite	0.62 - 0.77	3.13 NTU - 5.21 NTU	Lakes	Wuhan, China
Zhan et al. (2022)	C2X	0.64 - 0.73	1.5 NTU - 1.7 NTU	Hypersaline Coastal Lagoon	Mar Menor, Spain
Chowdhury et al. (2023)	Acolite	0.97 (r)	15.93 FNU	Guadalquivir Estuary	Gulf Cadiz, southern Spain
this study	Acolite	0.43	0.66 FNU	Sound/Coastal Zone	Reloncaví sound, NP, Chile

*is not indicated, only S2 satellite images are mentioned.

To know the turbidity status of water in a series of reservoirs Delegido et al. (2019) combined *in situ* measurements with Secchi disc depth with band ratios using different ACs obtaining a medium-to-high R^2 and low RMSE. Meanwhile, Zhan et al. (2022) applying similar techniques to estimate turbidity in a hypersaline coastal lagoon obtained similar R^2 and little error variations. Elhag et al. (2019) applied the

NDTI index, using the red and green bands obtained R^2 values higher than those reported in the aforementioned studies (Table 4). Consistent with these studies, our findings demonstrate acceptable R^2 values and minimal errors. However, it is important to consider that the results obtained with NDTI may have been influenced by the type of ecosystem, the presence of aquatic vegetation, and the high Chl-a content. This is mirrored in the study by Lizcano-Sandoval et al. (2022) where they applied the same index (NDTI) on S2 imagery in west-central Florida to map turbidity in covered seagrass.

This study uses spatial and temporal correspondence for the first time to evaluate the ACOLITE turbidity algorithms in a chilean marine ecosystem, which yield reasonably well correlated correspondences (r =0.63). Nechad et al. (2009) previously reported an RMSE around 5–7 FNU to estimate the turbidity from surface water sample measurements. In this study, using the Nv09 algorithm presented RMSE less than 0.66 FNU (see Figure 2a). On the other hand, Chowdhury et al. (2023) found a high correlation (r = 0.97) between *in situ* and satellite turbidity using S2 images in their research. The errors were close to 16 FNU, as shown in Table 4. Although the RMSE was higher than in this study, the algorithm was tested in a highly turbid area during extreme events. Therefore, the use of satellite imagery such as that derived from S2 (Vanhellemont and Ruddick, 2016) and advances in ACs algorithms (Vanhellemont and Ruddick, 2018, 2021) have opened new opportunities to gain insight into water quality variables with high spatial resolution and low errors. Research by Novoa et al. (2017), Kuhn et al. (2019), Caballero et al. (2020), Rodríguez-Benito et al. (2020), Vijay Prakash et al. (2021), Chowdhury et al. (2023), Paulista et al. (2023), Tavora et al. (2023a, 2023b) and also confirm the efficiency of ACOLITE as ACs in optically complex waters for the estimation of water quality parameters. Although we found that the Nechad algorithm implemented in ACOLITE is a good AC for turbidity estimation, future studies can implement other ACs, or other variants/techniques to estimate turbidity and complement the time series with other satellites such as Landsat 8 and Sentinel 3. Additionally, the evaluation and comparison of turbidity behavior in the spectral region of the Red-edge and Near-Infrared (NIR) at wavelengths between 705 nm and 865 nm should also be considered (see Table 1). Water turbidity can be sensitive to different wavelengths in this spectral range, as demonstrated by Chowdhury et al. (2023) in their research.

Remote sensing applications for aquaculture are promising tools to manage the challenges of ongoing climatic change (Snyder et al., 2017). Mussel aquaculture in NP is under challenges that threaten to disrupt the current pattern of climatic and environmental variability, including seasonal dynamics of environmental factors such as Chl-a, SS, CDOM, HABs, salinity, SST, pH, dissolved oxygen (DO), winds, turbidity, among others (Castillo et al., 2016; Curra-Sánchez et al., 2022; Iriarte et al., 2017, 2007; León-Muñoz et al., 2018; Molinet et al., 2015; Pantoja et al., 2011; Soto et al., 2019). Seasonal changes in

turbidity are evident, with maximum values during austral autumn for all years of our study period in association with changes in mean precipitation (e.g., autumn 2017, 2019, and 2020). This marked seasonality is typical as other environmental characteristics in temperate regions (Iriarte et al., 2007). Precipitation directly influences the outflow of water into the sound from the Puelo river, also reported by Aguayo et al. (2019) and León-Muñoz et al. (2013, 2021). The linkage between precipitation and large turbid plumes entering the Reloncaví sound was apparent in our study (see Figures 3, 6), and the results of Flores et al. (2022) confirm this behavior/pattern. Similar results were reported by Shen et al. (2021) and Mahmoud et al. (2023), in Asia, who showed that turbidity at the confluence of river tributaries or the highest concentrations of SS, Chl-a, and dissolved solids, respectively, were associated with heavy rainfall.

The turbid plumes to the greatest extent occurred in the autumn of 2019 and 2020, corresponding to the most severe storms and runoff events of the year and the highest turbidity value (27.96 FNU derived from Nv09 algorithm). The highest turbidity values appear coincident with the most pronounced discharge events occurring during 2019/05/02, and 2020/05/16, and 2020/05/25 (Figure 6 below). Conversely, less rainy seasons and negligible river discharges are often associated with areas of minimal plumes and low turbidity records (e.g., summer 2018). Therefore, the variation of maximum turbidity values seems to be influenced by the combination of precipitation and fluvial discharge from the river, especially in autumn.

Iriarte et al. (2017) reported changes in phytoplankton concentrations associated with intra-annual variability in the hydrological regime of the Puelo river during 2003-2011. Higher frequency of Chl-a and phytoplankton abundance in surface waters were observed when flows were lower than 350 m^3s^{-1}, coinciding with dry austral autumns during El Niño event (January-June). This resulted in a decoupling between outflows and satellite-measured Chl-a in surface waters during drier autumns. Similar results were found by Saldías et al. (2019) for the study area in the ISC seasonal climatology (2003-2019), reporting the maximum values of fluorescence (nFLH) in the austral autumn. Likewise, Vásquez et al. (2021) reported elevated Chl-a and nFLH peaks during the months of April, May and June 2018. The abundant Chl-a in the water in the austral autumn could be coincident with the elevated water turbidity found in our research (see Figure 6, SM1 Figure 4, 5b).

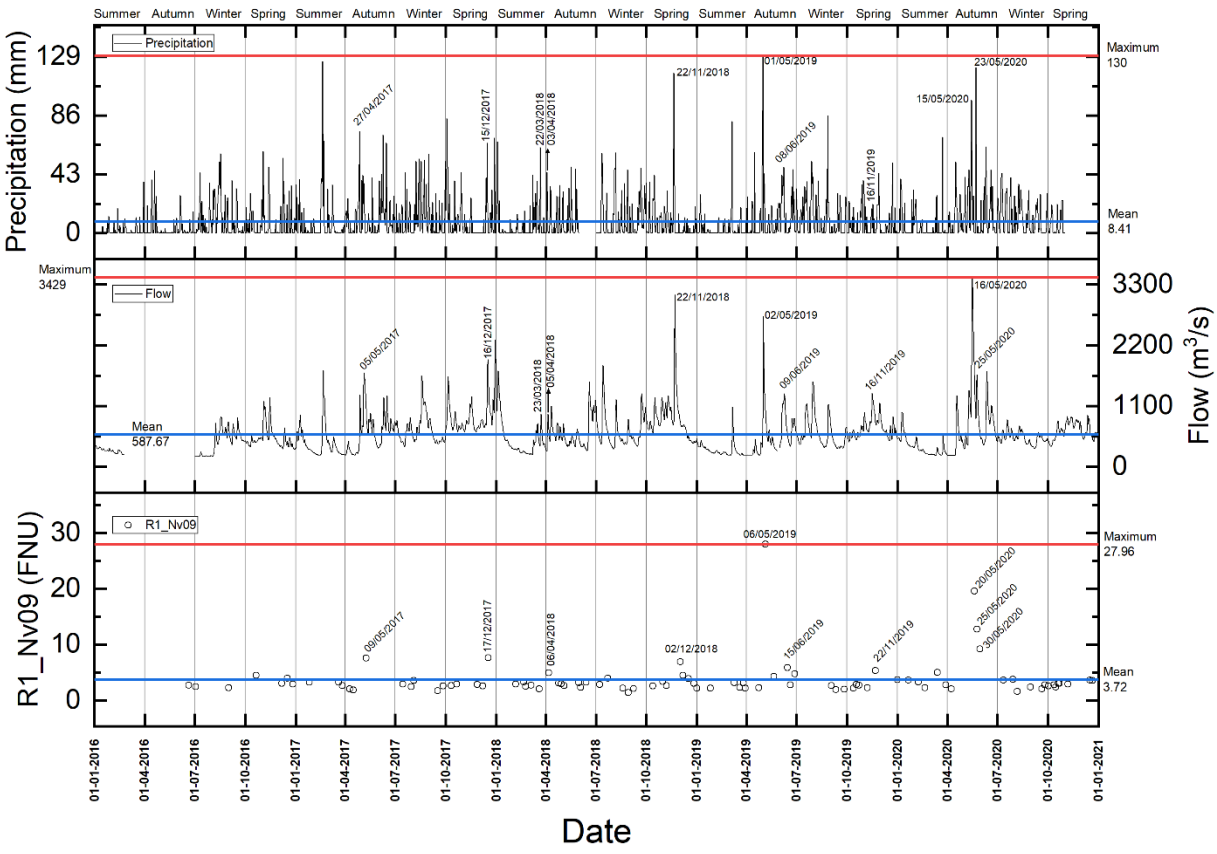

Figure 6. Time series of precipitation and river flow from DGA, and turbidity data at location R1 derived from the Nechad 2009 algorithm (Nv09).

The discharge and influence area of the river plume increases turbidity in the coastal zone, and this study confirms that this behavior is maintained over time (see Figure 4, 6). The highest turbidity values were found in site R1 (27.96 FNU) followed by site R2 (19.55 FNU). Both sites are distributed in river (R1), and river mouth (R2). In this sense, Curra-Sánchez et al. (2022) for ISC basins indicated that turbid waters in the river and estuary were caused by high concentrations of CDOM from river discharge, mainly of allochthonous origin. Given the strong relationship between turbidity and total suspended matter (R^2= 0.82), Chowdhury et al. (2023) showed that in-stream and estuarine sites had the highest turbidity values consistent with that reported in this study. Aguayo et al. (2019) through hydrological models estimated future scenarios where they found a trend of high discharge of the Puelo river in May, June, July, also influenced by abundant rainfall. We foresee that in the future this situation could lead to high turbidity in the river plume as we found in this study. It was found that the sites farthest from this influence, such as R4 and R5, had low turbidity during most of the time series, while the sites close to the river had high

turbidity values. Our results show that as we move away from this zone of influence of the river discharge, turbidity decreases, as was the case at sites R4 and R5 (see Figure 4). However, on some occasions in austral autumn both sites recorded values close to 5 FNU (see SM1 Table 4). This may be due to high river discharge and strong winds that move the plume to areas close to both sites (Flores et al., 2022).

Figure 7 shows the wind compass 72 hours before S2 image acquisition for the four high turbidity images. The first three dates provide evidence that the highest frequency (>30%) corresponds to northerly wind with speeds above 4 kt (7.2 km/h), coincident with t increasing turbidity in the seaward sites. Similar results have been reported by Banas et al. (2005), Hyun (2007), Abirhire et al. (2020), Rodríguez-López et al. (2022). For example, Banas et al. (2005) in their study found strong relationships between wind and SS concentration, indicating that increasing wind speed can lead to re-suspension of particles in water. The results of Abirhire et al. (2020) also show that there is a strong influence of winds to generate turbid waters. The direction and intensity of the wind can influence the river plume, as shown in Figure 7. When the wind blows from the north, the plume is pushed towards the south, and vice versa. Therefore, the study area is impacted by the strong winds present throughout the year. This suggests that winds could be transferring SS, CDOM, and particulate matter from the river discharge and coastal zone to R4 and R5, which could increase turbidity at both sites.

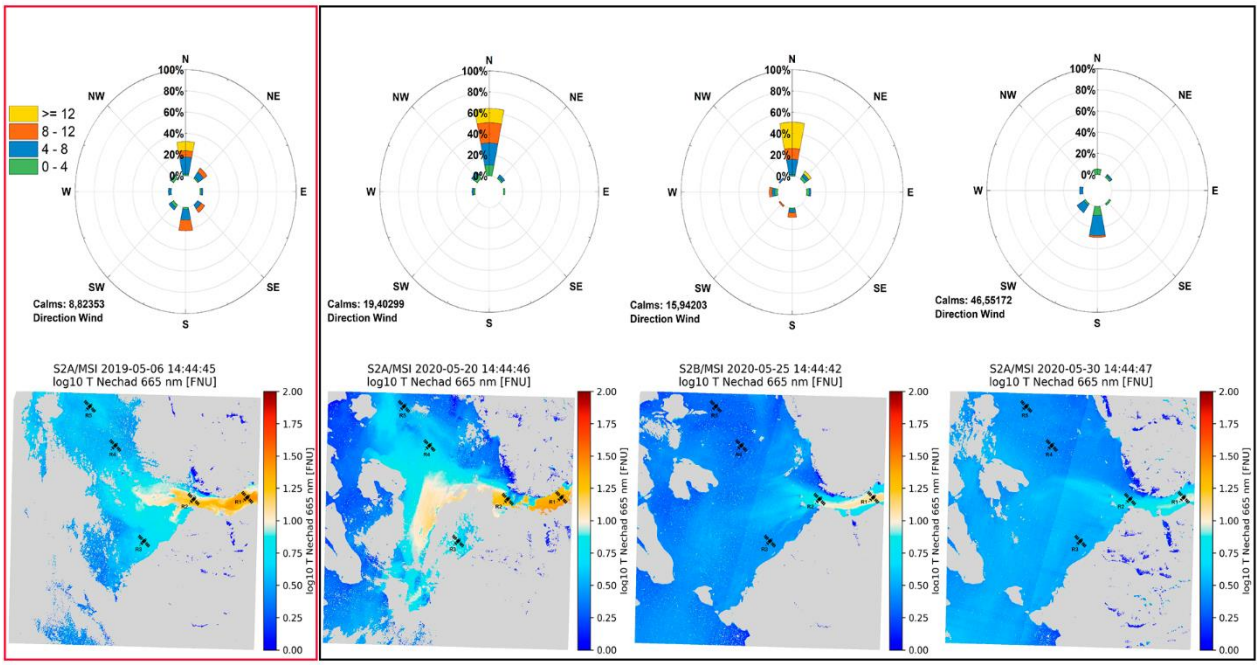

Figure 7. The top panel shows wind rose corresponding to 72 hours before S2 imagen acquisition and the bottom panel shows results from the Nv09 algorithm for autumn days. The panel in red shows the image from the date with the highest turbidity on 2019/05/06. The panel in black shows the images from 2020/05/20, 2020/05/25 and 2020/05/30.

Several studies have shown that anthropogenic activities, such as land use and land use change, aquaculture, and marine traffic, can have a significant impact on water quality (Broitman et al., 2017; Lara et al., 2018; León-Muñoz et al., 2021; Pérez et al., 2015). Curra-Sánchez et al. (2022) observed that the basin with predominantly agricultural use has a greater availability and quantity of nutrients, specifically nitrates and phosphates, due to the use of agricultural fertilizers. In contrast, the basin with a larger area of native forest registered high values of CDOM. Adjacent basins through surface runoff can contribute large amounts of organic matter and nutrients, such as agricultural or forestry wastes, causing water turbidity due to accelerated growth of algae, algal blooms and HABs on the surface and in the water column (Bilotta and Brazier, 2008; Doan et al., 2015; Hudson and Vandergucht, 2015; Pérez-Ruzafa et al., 2019). Mahmoud et al. (2023) demonstrate that there is a relationship between water temperature and Chl-a, this relationship may be influenced by the availability of sunlight, which directly affects phytoplankton growth. In austral summer 2016, León-Muñoz et al. (2018) detected an active HABs in NP that wiped out almost 12% of Chilean salmon production, this was produced by increased SST and lower freshwater input, generating more saline and nutrient-rich waters, coinciding with a strong El Niño event.

Similar results were reported by Soto et al. (2019) in salmon farming districts in the Reloncaví sound, where the combination of decreased rainfall and DO, and the development of HABs impacted the production of this species. On the other hand, Sandoval et al. (2018) also reported the occurrence of HABs in austral spring and austral autumn in the study area. Rodríguez-Benito et al. (2020) through remote sensing with S2 images detected the presence of HABs in March and April 2020 in ISC. Turbid waters with the presence of HABs impact not only water quality and clarity, but also the habitat of organisms. According to these environmental conditions, sites R4 and R5 have favorable locations for the development of HABs. However, in some seasons of the year, due to the scarce fluvial discharge, all the sites in our study present conditions for the development of HABs.

During the covid-19 years, authors such as Rodriguez-Benito et al. (2020), Sun et al. (2021) and Vijay Prakash et al. (2021) studied the behavior of water quality in different aquatic ecosystems using satellite images. Sun et al. (2021) found that water turbidity decreased at the beginning of 2020 in the lakes they studied, the model they obtained for S2 presented an R^2=0.67, however, they found that both lakes during the period December 2019 to February 2020 decreased R^2= 0.46 and R^2= 0.37. Mean turbidity values decreased from 33 NTU to 25 NTU, implying that the decrease in anthropogenic activities due to the covid-19 closure had an impact on water turbidity. Although in our study area there was a decrease in turbidity for these same dates (December 2019 - February 2020), in general in 2019 there was a predominance of turbid waters in the Reloncaví sound, due to the complex processes that occur here such as algal blooms, strong winds and fluvial discharges, which cause the clarity and quality of the water in this ecosystem to fluctuate.

Considering that aquaculture is the main economic activity in the Reloncaví area, this type of study is extremely important for continuous monitoring and warning of increases in water turbidity in real time. Our results provide valuable information on the spatio-temporal dynamics of turbidity in Reloncaví sound, underscoring the need for comprehensive monitoring strategies to understand and manage water quality parameters in the study area.

5. CONCLUSIONES

The Copernicus data's availability and easy access enabled the evaluation of turbidity behavior at spatial high resolution in Reloncaví sound. This study uses spatial and temporal correspondence for the first time to evaluate the ACOLITE turbidity algorithms in a chilean marine ecosystem. The Nv09 algorithm would be more reliable than the Nv16 algorithm for developing a future predictor model of turbidity. Heavy rainfall caused high river discharges, which in turn influenced the turbidity in the Reloncaví sound. Austral autumn (May) was characterized by the highest turbidity values. Site R1 (river) and R5 (away from the influence of river discharges) recorded the highest and lowest turbidity values, respectively. This study contributes to early warning of the occurrence of high turbidity events due to river discharge and the development of HABs to promote future actions that encourage sustainable management of the coastal zone, thus avoiding economic losses and effective control and management of aquaculture areas.

REFERENCIAS BIBLIOGRÁFICAS

Aavaste, A., Sipelgas, L., Uiboupin, R., Uudeberg, K., 2021. Impact of Thermohaline Conditions on Vertical Variability of Optical Properties in the Gulf of Finland (Baltic Sea): Implications for Water Quality Remote Sensing. Front Mar Sci 8, 537. https://doi.org/10.3389/FMARS.2021.674065/

Abirhire, O., Davies, J.M., Guo, X., Hudson, J., 2020. Understanding the factors associated with long-term reconstructed turbidity in Lake Diefenbaker from Landsat-imagery. Science of the Total Environment 724. https://doi.org/10.1016/J.SCITOTENV.2020.138222

Aguayo, R., León-Muñoz, J., Vargas-Baecheler, J., Montecinos, A., Garreaud, R., Urbina, M., Soto, D., Iriarte, J.L., 2019. The glass half-empty: climate change drives lower freshwater input in the coastal system of the Chilean Northern Patagonia. Climatic Change 2019 155:3 155, 417–435. https://doi.org/10.1007/S10584-019-02495-6

Alvado, B., Sòria-Perpinyà, X., Vicente, E., Delegido, J., Urrego, P., Ruíz-Verdú, A., Soria, J.M., Moreno, J., 2021. Estimating organic and inorganic part of suspended solids from sentinel 2 in different inland waters. Water (Switzerland) 13. https://doi.org/10.3390/W13182453

Anderson, C.W., 2005. Turbidity (ver.2.1): U.S. Geological Survey Techniques of Water-Resources Investigations, book 9, chap. A6, sec 6.7, Techniques of Water-Resources Investigations. Reston, VA. https://doi.org/10.3133/twri09A6.7

Anderson, D.M., Cembella, A.D., Hallegraeff, G.M., 2012. Progress in understanding harmful algal blooms: Paradigm shifts and new technologies for research, monitoring, and management. Ann Rev Mar Sci 4, 143–176. https://doi.org/10.1146/ANNUREV-MARINE-120308-081121

Aragonés, L., Pagán, J.I., López, M.P., García-Barba, J., 2016. The impacts of Segura River (Spain) channelization on the coastal seabed. Science of the Total Environment 543, 493–504. https://doi.org/10.1016/j.scitotenv.2015.11.058

Astorga, M.P., Vargas, J., Valenzuela, A., Molinet, C., Marín, S.L., 2018. Population genetic structure and differential selection in mussel Mytilus chilensis. Aquac Res 49, 919–927. https://doi.org/10.1111/ARE.13538

Babin, M., Stramski, D., Ferrari, G.M., Claustre, H., Bricaud, A., Obolensky, G., Hoepffner, N., 2003. Variations in the light absorption coefficients of phytoplankton, nonalgal particles, and dissolved organic matter in coastal waters around Europe. J Geophys Res Oceans 108. https://doi.org/10.1029/2001JC000882

Balasubramanian, S. V., Pahlevan, N., Smith, B., Binding, C., Schalles, J., Loisel, H., Gurlin, D., Greb, S., Alikas, K., Randla, M., Bunkei, M., Moses, W., Nguyễn, H., Lehmann, M.K., O'Donnell, D., Ondrusek, M., Han, T.H., Fichot, C.G., Moore, T., Boss, E., 2020. Robust algorithm for estimating total suspended solids (TSS) in inland and nearshore coastal waters. Remote Sens Environ 246. https://doi.org/10.1016/J.RSE.2020.111768

Banas, D., Grillas, P., Auby, I., Lescuyer, F., Coulet, E., Moreteau, J.C., Millet, B., 2005. Short time scale changes in underwater irradiance in a wind-exposed lagoon (Vaccarès lagoon, France): Efficiency of infrequent field measurements of water turbidity or weather data to predict irradiance in the water column. Hydrobiologia 551, 3–16. https://doi.org/10.1007/S10750-005-4446-1

Barragán, J.M., de Andrés, M., 2015. Analysis and trends of the world's coastal cities and agglomerations. Ocean Coast Manag 114, 11–20. https://doi.org/10.1016/J.OCECOAMAN.2015.06.004

Barria, A., Gebauer, P., Molinet, C., 2012. Variabilidad espacial y temporal del suministro larval de mitílidos en el Seno de Reloncaví, sur de Chile. Rev Biol Mar Oceanogr 47, 461–473. https://doi.org/10.4067/s0718-19572012000300009

Bilotta, G.S., Brazier, R.E., 2008. Understanding the influence of suspended solids on water quality and aquatic biota. Water Res 42, 2849–2861. https://doi.org/10.1016/J.WATRES.2008.03.018

Brando, V.E., Braga, F., Zaggia, L., Giardino, C., Bresciani, M., Matta, E., Bellafiore, D., Ferrarin, C., Maicu, F., Benetazzo, A., Bonaldo, D., Falcieri, F.M., Coluccelli, A., Russo, A., Carniel, S., 2015. High-resolution

satellite turbidity and sea surface temperature observations of river plume interactions during a significant flood event. Ocean Science 11, 909–920. https://doi.org/10.5194/OS-11-909-2015

Broitman, B.R., Halpern, B.S., Gelcich, S., Lardies, M.A., Vargas, C.A., Vásquez-Lavín, F., Widdicombe, S., Birchenough, S.N.R., 2017. Dynamic interactions among boundaries and the expansion of sustainable aquaculture. Front Mar Sci 4. https://doi.org/10.3389/FMARS.2017.00015

Budhiman, S., Suhyb Salama, M., Vekerdy, Z., Verhoef, W., 2012. Deriving optical properties of Mahakam Delta coastal waters, Indonesia using in situ measurements and ocean color model inversion. ISPRS Journal of Photogrammetry and Remote Sensing 68, 157–169. https://doi.org/10.1016/J.ISPRSJPRS.2012.01.008

Buschmann, A., Cabello, F., Young, K., Carvajal, J., Varela, D.A., Henríquez, L., 2009. Salmon aquaculture and coastal ecosystem health in Chile: Analysis of regulations, environmental impacts and bioremediation systems. Ocean Coast Manag 52, 243–249. https://doi.org/10.1016/J.OCECOAMAN.2009.03.002

Buschmann, A., Niklitschek, E.J., Pereda, S. V, 2021. Aquaculture and its impacts on the conservation of Chilean Patagonia, in: Castilla, J.C., Armesto, J.J., Martínez-Harms, M.J. (Eds.), Conservación En La Patagonia Chilena: Evaluación Del Conocimiento, Oportunidades y Desafíos. Ediciones Universidad Católica, Santiago, Chile, p. 600.

Caballero, I., Fernández, R., Escalante, O.M., Mamán, L., Navarro, G., 2020. New capabilities of Sentinel-2A/B satellites combined with in situ data for monitoring small harmful algal blooms in complex coastal waters. Sci Rep 10. https://doi.org/10.1038/S41598-020-65600-1

Caballero, I., Ruiz, J., Navarro, G., 2019. Sentinel-2 satellites provide near-real time evaluation of catastrophic floods in the West Mediterranean. Water (Switzerland) 11. https://doi.org/10.3390/W11122499

Caballero, I., Steinmetz, F., Navarro, G., 2018. Evaluation of the first year of operational Sentinel-2A data for retrieval of suspended solids in medium- to high-turbiditywaters. Remote Sens (Basel) 10. https://doi.org/10.3390/RS10070982

Caballero, I., Stumpf, R.P., 2020. Towards routine mapping of shallow bathymetry in environments with variable turbidity: Contribution of sentinel-2A/B satellites mission. Remote Sens (Basel) 12. https://doi.org/10.3390/RS12030451

Camelo-Guarín, S., Molinet, C., Soto, D., 2021. Recommendations for implementing integrated multitrophic aquaculture in commercial farms at the landscape scale in southern Chile. Aquaculture 544, 737116. https://doi.org/10.1016/J.AQUACULTURE.2021.737116

Castillo, M.I., Cifuentes, U., Pizarro, O., Djurfeldt, L., Caceres, M., 2016. Seasonal hydrography and surface outflow in a fjord with a deep sill: the Reloncaví fjord, Chile. Ocean Sci 12, 533–534. https://doi.org/10.5194/os-12-533-2016

Chowdhury, M., Vilas, C., van Bergeijk, S., Navarro, G., Laiz, I., Caballero, I., 2023. Monitoring turbidity in a highly variable estuary using Sentinel 2-A/B for ecosystem management applications. Front Mar Sci 10, 1186441. https://doi.org/10.3389/FMARS.2023.1186441/BIBTEX

Ciancia, E., Campanelli, A., Lacava, T., Palombo, A., Pascucci, S., Pergola, N., Pignatti, S., Satriano, V., Tramutoli, V., 2020. Modeling and multi-temporal characterization of total suspended matter by the combined use of sentinel 2-MSI and landsat 8-OLI Data: The Pertusillo lake case study (Italy). Remote Sens (Basel) 12. https://doi.org/10.3390/RS12132147

Claverie, M., Ju, J., Masek, J.G., Dungan, J.L., Vermote, E.F., Roger, J.C., Skakun, S. V., Justice, C., 2018. The Harmonized Landsat and Sentinel-2 surface reflectance data set. Remote Sens Environ 219, 145–161. https://doi.org/10.1016/J.RSE.2018.09.002

Cloern, J.E., 1987. Turbidity as a control on phytoplankton biomass and productivity in estuaries. Cont Shelf Res 7, 1367–1381. https://doi.org/10.1016/0278-4343(87)90042-2

Curra-Sánchez, E.D., Lara, C., Cornejo-D'Ottone, M., Nimptsch, J., Aguayo, M., Broitman, B.R., Saldías, G.S., Vargas, C.A., 2022. Contrasting land-uses in two small river basins impact the colored dissolved organic matter concentration and carbonate system along a river-coastal ocean continuum. Science of The Total Environment 806, 150435. https://doi.org/10.1016/J.SCITOTENV.2021.150435

Davies-Colley, R.J., Smith, D.G., 2001. Turbidity, suspended sediment, and water clarity: a review. JAWRA Journal of the American Water Resources Association 37, 1085–1101. https://doi.org/10.1111/J.1752-1688.2001.TB03624.X

de Castro Medeiros, L., Mattos, A., Lürling, M., Becker, V., 2015. Is the future blue-green or brown? The effects of extreme events on phytoplankton dynamics in a semi-arid man-made lake. Aquat Ecol 49, 293–307. https://doi.org/10.1007/S10452-015-9524-5/FIGURES/8

Delegido, J., Urrego, P., Vicente, E., Sòria-Perpinyà, X., Soria, J.M., Pereira-Sandoval, M., Ruiz-Verdú, A., Peña, R., Moreno, J., 2019. Turbidity and Secchi disc depth with Sentinel-2 in different trophic status reservoirs at the Comunidad Valenciana. Revista de Teledetección 2019, 15–24. https://doi.org/10.4995/RAET.2019.12603

Díaz, P.A., Álvarez, G., Varela, D., Pérez-Santos, I., Díaz, M., Molinet, C., Seguel, M., Aguilera-Belmonte, A., Guzmán, L., Uribe, E., Rengel, J., Hernández, C., Segura, C., Figueroa, R.I., 2019. Impacts of harmful algal blooms on the aquaculture industry: Chile as a case study. Perspectives in Phycology 6, 39–50. https://doi.org/10.1127/PIP/2019/0081

Díaz, P.A., Figueroa, R.I., 2023. Toxic Algal Bloom Recurrence in the Era of Global Change: Lessons from the Chilean Patagonian Fjords. Microorganisms 2023, Vol. 11, Page 1874 11, 1874. https://doi.org/10.3390/MICROORGANISMS11081874

Doan, P.T.K., Némery, J., Schmid, M., Gratiot, N., 2015. Eutrophication of turbid tropical reservoirs: Scenarios of evolution of the reservoir of Cointzio, Mexico. Ecol Inform 29, 192–205. https://doi.org/10.1016/J.ECOINF.2015.01.006

Dogliotti, A.I., Ruddick, K.G., Nechad, B., Doxaran, D., Knaeps, E., 2015. A single algorithm to retrieve turbidity from remotely-sensed data in all coastal and estuarine waters. Remote Sens Environ 156, 157–168. https://doi.org/10.1016/J.RSE.2014.09.020

Duckey, T., Lewis, M., Chang, G., 2006. Optical oceanography: Recent advances and future directions using global remote sensing and in situ observations. Reviews of Geophysics 44. https://doi.org/10.1029/2003RG000148

Elhag, M., Gitas, I., Othman, A., Bahrawi, J., Gikas, P., 2019. Assessment of Water Quality Parameters Using Temporal Remote Sensing Spectral Reflectance in Arid Environments, Saudi Arabia. Water 2019, Vol. 11, Page 556 11, 556. https://doi.org/10.3390/W11030556

ESA - European Space Agency, 2015. Sentinel-2 User Handbook. ESA Standard Document. European Space Agency. París.

FAO, 2022. The State of World Fisheries and Aquaculture 2022. Towards Blue Transformation. https://doi.org/10.4060/CC0461EN

Flores, R.P., Lara, C., Saldías, G.S., Vásquez, S.I., Roco, A., 2022. Spatio-temporal variability of turbid freshwater plumes in the Inner Sea of Chiloé, northern Patagonia. Journal of Marine Systems 228, 103709. https://doi.org/10.1016/J.JMARSYS.2022.103709

Frantz, D., 2019. FORCE-Landsat + Sentinel-2 analysis ready data and beyond. Remote Sens (Basel) 11. https://doi.org/10.3390/RS11091124

Garreaud, R., 2018. Record-breaking climate anomalies lead to severe drought and environmental disruption in western Patagonia in 2016. Clim Res 74, 217–229. https://doi.org/10.3354/cr01505

Garreaud, R., Lopez, P., Minvielle, M., Rojas, M., 2013. Large-scale control on the Patagonian climate. J Clim 26, 215–230. https://doi.org/10.1175/jcli-d-12-00001.1

GEBCO Gridded Bathymetry Data [WWW Document], n.d. URL https://www.gebco.net/data_and_products/gridded_bathymetry_data/ (accessed 4.25.23).

Gelda, R.K., Effler, S.W., Prestigiacomo, A.R., Peng, F., Effler, A.J.P., Wagner, B.A., Perkins, M.G., O'Donnell, D.M., O'Donnell, S.M., Pierson, D.C., 2013. Characterizations and modeling of turbidity in a water supply reservoir following an extreme runoff event. Inland Waters 3, 377–390. https://doi.org/10.5268/IW-3.3.581

Grobbelaar, J.U., 2009. Turbidity. Encyclopedia of Inland Waters 699–704. https://doi.org/10.1016/B978-012370626-3.00075-2

Harmel, T., Chami, M., Tormos, T., Reynaud, N., Danis, P.A., 2018. Sunglint correction of the Multi-Spectral Instrument (MSI)-SENTINEL-2 imagery over inland and sea waters from SWIR bands. Remote Sens Environ 204, 308–321. https://doi.org/10.1016/J.RSE.2017.10.022

Hudson, J.J., Vandergucht, D.M., 2015. Spatial and temporal patterns in physical properties and dissolved oxygen in Lake Diefenbaker, a large reservoir on the Canadian Prairies. J Great Lakes Res 41, 22–33. https://doi.org/10.1016/J.JGLR.2015.06.007

Hyun, J.C., 2007. Effects of prevailing winds on turbidity of a shallow estuary. Int J Environ Res Public Health 4, 185–192. https://doi.org/10.3390/IJERPH2007040014

Iriarte, J.L., González, H.E., Liu, K.K., Rivas, C., Valenzuela, C., 2007. Spatial and temporal variability of chlorophyll and primary productivity in surface waters of southern Chile (41.5–43° S). Estuar Coast Shelf Sci 74, 471–480. https://doi.org/10.1016/J.ECSS.2007.05.015

Iriarte, J.L., León-Muñoz, J., Marcé, R., Clément, A., Lara, C., 2017. Influence of seasonal freshwater streamflow regimes on phytoplankton blooms in a Patagonian fjord. New Zeal J Mar Freshw Res 51, 304–315. https://doi.org/10.1080/00288330.2016.1220955

Iriarte, J.L., Pantoja, S., Daneri, G., Iriarte, J.L., Pantoja, S., Daneri, G., 2014. Oceanographic Processes in Chilean Fjords of Patagonia: From small to large-scale studies. Prog Oceanogr 129, 1–7. https://doi.org/10.1016/J.POCEAN.2014.10.004

Jerlov, N.G., 1957. A Transparency-Meter for Ocean Water. Tellus 9, 229–233. https://doi.org/10.1111/J.2153-3490.1957.TB01877.X

Khan, R.M., Salehi, B., Mahdianpari, M., Mohammadimanesh, F., Mountrakis, G., Quackenbush, L.J., 2021. A Meta-Analysis on Harmful Algal Bloom (HAB) Detection and Monitoring: A Remote Sensing Perspective. Remote Sensing 2021, Vol. 13, Page 4347 13, 4347. https://doi.org/10.3390/RS13214347

Kirk, J.T.O., 1985. Effects of suspensoids (turbidity) on penetration of solar radiation in aquatic ecosystems. Hydrobiologia 125, 195–208. https://doi.org/10.1007/BF00045935

Kirk, J.T.O., 1984. Dependence of relationship between inherent and apparent optical properties of water on solar altitude. Limnol Oceanogr 29, 350–356. https://doi.org/10.4319/LO.1984.29.2.0350

Kuhn, C., de Matos Valerio, A., Ward, N., Loken, L., Sawakuchi, H.O., Kampel, M., Richey, J., Stadler, P., Crawford, J., Striegl, R., Vermote, E., Pahlevan, N., Butman, D., 2019. Performance of Landsat-8 and Sentinel-2 surface reflectance products for river remote sensing retrievals of chlorophyll-a and turbidity. Remote Sens Environ 224, 104–118. https://doi.org/10.1016/j.rse.2019.01.023

Lara, C., Miranda, M., Montecino, V., Iriarte, J.L., 2010. Chlorophyll-a MODIS mesoscale variability in the Inner Sea of Chiloé, Patagonia, Chile (41-43°S): Patches and Gradients? Rev Biol Mar Oceanogr 45, 217–225. https://doi.org/10.4067/S0718-19572010000200003

Lara, C., Saldías, G.S., Paredes, A.L., Cazelles, B., Broitman, B.R., 2018. Temporal Variability of MODIS Phenological Indices in the Temperate Rainforest of Northern Patagonia. Remote Sensing 2018, Vol. 10, Page 956 10, 956. https://doi.org/10.3390/RS10060956

Lara, C., Saldías, G.S., Tapia, F.J., Iriarte, J.L., Broitman, B.R., 2016. Interannual variability in temporal patterns of Chlorophyll–a and their potential influence on the supply of mussel larvae to inner waters in northern Patagonia (41–44°S). Journal of Marine Systems 155, 11–18. https://doi.org/10.1016/J.JMARSYS.2015.10.010

Lee, H.W., Kim, E.J., Park, S.S., Choi, J.H., 2015. Effects of Climate Change on the Movement of Turbidity Flow in a Stratified Reservoir. Water Resources Management 29, 4095–4110. https://doi.org/10.1007/S11269-015-1047-2/FIGURES/7

Lee, Z., Carder, K.L., Arnone, R.A., 2002. Deriving inherent optical properties from water color: a multiband quasi-analytical algorithm for optically deep waters. Applied Optics, Vol. 41, Issue 27, pp. 5755-5772 41, 5755–5772. https://doi.org/10.1364/AO.41.005755

León-Muñoz, J., Aguayo, R., Marcé, R., Catalán, N., Woelfl, S., Nimptsch, J., Arismendi, I., Contreras, C., Soto, D., Miranda, A., 2021. Climate and Land Cover Trends Affecting Freshwater Inputs to a Fjord in Northwestern Patagonia. Front Mar Sci 8, 960. https://doi.org/10.3389/FMARS.2021.628454/BIBTEX

León-Muñoz, J., Marcé, R., Iriarte, J.L., 2013. Influence of hydrological regime of an Andean river on salinity, temperature and oxygen in a Patagonia fjord, Chile. New Zeal J Mar Freshw Res 47, 515–528. https://doi.org/10.1080/00288330.2013.802700

León-Muñoz, J., Urbina, M.A., Garreaud, R., Iriarte, J.L., 2018. Hydroclimatic conditions trigger record harmful algal bloom in western Patagonia (summer 2016). Sci Rep 8, 1330. https://doi.org/10.1038/s41598-018-19461-4

Lizcano-Sandoval, L., Anastasiou, C., Montes, E., Raulerson, G., Sherwood, E., Muller-Karger, F.E., 2022. Seagrass distribution, areal cover, and changes (1990–2021) in coastal waters off West-Central Florida, USA. Estuar Coast Shelf Sci 279, 108134. https://doi.org/10.1016/J.ECSS.2022.108134

Magrì, S., Ottaviani, E., Prampolini, E., Federici, B., Besio, G., Fabiano, B., 2023. Application of machine learning techniques to derive sea water turbidity from Sentinel-2 imagery. Remote Sens Appl 30, 100951. https://doi.org/10.1016/J.RSASE.2023.100951

Mahmoud, S.H., S. Ahmed, S., Zhu, D.Z., Gan, T.Y., Loewen, M.R., van Duin, B., Mahmood, K., 2023. Monitoring the spatial distribution of water quality of an urban stormwater pond using satellite images. Ecol Inform 77, 102205. https://doi.org/10.1016/J.ECOINF.2023.102205

Mélin, F., Vantrepotte, V., 2015. How optically diverse is the coastal ocean? Remote Sens Environ 160, 235–251. https://doi.org/10.1016/J.RSE.2015.01.023

Mendes, R., Vaz, N., Fernández-Nóvoa, D., Da Silva, J.C.B., DeCastro, M., Gómez-Gesteira, M., Dias, J.M., 2014. Observation of a turbid plume using MODIS imagery: The case of Douro estuary (Portugal). Remote Sens Environ 154, 127–138. https://doi.org/10.1016/J.RSE.2014.08.003

Mobley, C.D., 2022. The Oceanic Optics Book. International Ocean Colour Coordinating Group (IOCCG) Dartmouth, NS, Canada 924. https://doi.org/10.25607/OBP-1710

Mobley, C.D., 2001. Radiative Transfer in the Ocean. Encyclopedia of Ocean Sciences 2321–2330. https://doi.org/10.1006/RWOS.2001.0469

Molinet, C., Astorga, M., Cares, L., Diaz, M., Hueicha, K., Marín, S., Matamala, T., Soto, D., 2021. Vertical distribution patterns of larval supply and spatfall of three species of Mytilidae in a Chilean fjord used for mussel farming: Insights for mussel spatfall efficiency. Aquaculture 535, 736341. https://doi.org/10.1016/J.AQUACULTURE.2021.736341

Molinet, C., Díaz Gomez, M.A., Arriagada Muñoz, C.B., Cares Pérez, L.E., Marín Arribas, S.L., Astorga Opazo, M.P., Niklitschek Huaquin, E.J.E., 2015. Spatial distribution pattern of Mytilus chilensis beds in the Reloncaví fjord: Hypothesis on associated processes. Revista Chilena de Historia Natural 88, 1–12. https://doi.org/10.1186/S40693-015-0041-7/

Morel, A., Gentili, B., 1993. Diffuse reflectance of oceanic waters II Bidirectional aspects. Appl Opt 32, 6864. https://doi.org/10.1364/AO.32.006864

Morel, A., Prieur, L., 1977. Analysis of variations in ocean color. Limnol Oceanogr 22, 709–722. https://doi.org/10.4319/LO.1977.22.4.0709

Nechad, B., Ruddick, K.G., Neukermans, G., 2009. Calibration and validation of a generic multisensor algorithm for mapping of turbidity in coastal waters. Remote Sensing of the Ocean, Sea Ice, and Large Water Regions 2009 7473, 74730H. https://doi.org/10.1117/12.830700

Nechad, B., Ruddick, K.G., Park, Y., 2010. Calibration and validation of a generic multisensor algorithm for mapping of total suspended matter in turbid waters. Remote Sens Environ 114, 854–866. https://doi.org/10.1016/J.RSE.2009.11.022

Novoa, S., Doxaran, D., Ody, A., Vanhellemont, Q., Lafon, V., Lubac, B., Gernez, P., 2017. Atmospheric corrections and multi-conditional algorithm for multi-sensor remote sensing of suspended particulate matter in low-to-high turbidity levels coastal waters. Remote Sens (Basel) 9. https://doi.org/10.3390/RS9010061

Odermatt, D., Gitelson, A., Brando, V.E., Schaepman, M., 2012. Review of constituent retrieval in optically deep and complex waters from satellite imagery. Remote Sens Environ 118, 116–126. https://doi.org/10.1016/J.RSE.2011.11.013

Pahlevan, N., Mangin, A., Balasubramanian, S. V., Smith, B., Alikas, K., Arai, K., Barbosa, C., Bélanger, S., Binding, C., Bresciani, M., Giardino, C., Gurlin, D., Fan, Y., Harmel, T., Hunter, P., Ishikaza, J., Kratzer, S., Lehmann, M.K., Ligi, M., Ma, R., Martin-Lauzer, F.R., Olmanson, L., Oppelt, N., Pan, Y., Peters, S., Reynaud, N., Sander de Carvalho, L.A., Simis, S., Spyrakos, E., Steinmetz, F., Stelzer, K., Sterckx, S., Tormos, T., Tyler, A., Vanhellemont, Q., Warren, M., 2021. ACIX-Aqua: A global assessment of atmospheric correction methods for Landsat-8 and Sentinel-2 over lakes, rivers, and coastal waters. Remote Sens Environ 258. https://doi.org/10.1016/J.RSE.2021.112366

Pahlevan, N., Smith, B., Binding, C., O'Donnell, D.M., 2017. Spectral band adjustments for remote sensing reflectance spectra in coastal/inland waters. Opt Express 25, 28650. https://doi.org/10.1364/OE.25.028650

Pantoja, S., Iriarte, J.L., Daneri, G., 2011. Oceanography of the Chilean Patagonia. Cont Shelf Res 31, 149–153. https://doi.org/10.1016/J.CSR.2010.10.013

Paulista, R.S.D., de Almeida, F.T., de Souza, A.P., Hoshide, A.K., de Abreu, D.C., da Silva Araujo, J.W., Martim, C.C., 2023. Estimating Suspended Sediment Concentration Using Remote Sensing for the Teles Pires River, Brazil. Sustainability 2023, Vol. 15, Page 7049 15, 7049. https://doi.org/10.3390/SU15097049

Pérez, C.A., DeGrandpre, M.D., Lagos, N.A., Saldías, G.S., Cascales, E.K., Vargas, C.A., 2015. Influence of climate and land use in carbon biogeochemistry in lower reaches of rivers in central southern Chile: Implications for the carbonate system in river-influenced rocky shore environments. J Geophys Res Biogeosci 120, 673–692. https://doi.org/10.1002/2014JG002699

Pérez-Ruzafa, A., Campillo, S., Fernández-Palacios, J.M., García-Lacunza, A., García-Oliva, M., Ibañez, H., Navarro-Martínez, P.C., Pérez-Marcos, M., Pérez-Ruzafa, I.M., Quispe-Becerra, J.I., Sala-Mirete, A., Sánchez, O., Marcos, C., 2019. Long-term dynamic in nutrients, chlorophyll a, and water quality parameters in a coastal lagoon during a process of eutrophication for decades, a sudden break and a relatively rapid recovery. Front Mar Sci 6, 26. https://doi.org/10.3389/FMARS.2019.00026/BIBTEX

Pérez-Santos, I., Díaz, P.A., Silva, N., Garreaud, R., Montero, P., Henríquez-Castillo, C., Barrera, F., Linford, P., Amaya, C., Contreras, S., Aracena, C., Pinilla, E., Altamirano, R., Vallejos, L., Pavez, J., Maulen, J., 2021. Oceanography time series reveals annual asynchrony input between oceanic and estuarine waters in Patagonian fjords. Science of The Total Environment 798, 149241. https://doi.org/10.1016/J.SCITOTENV.2021.149241

Pérez-Santos, I., Seguel, R., Schneider, W., Linford, P., Donoso, D., Navarro, E., Amaya-Cárcamo, C., Pinilla, E., Daneri, G., 2019. Synoptic-scale variability of surface winds and ocean response to atmospheric forcing in the eastern austral pacific ocean. Ocean Science 15, 1247–1266. https://doi.org/10.5194/OS-15-1247-2019

Phuoc Hoang Son, T., Lau, K., Minh-Thu, P., 2013. The inherent optical properties (IOPs) algorithms for detection the water quality in turbid waters of Mekong estuaries. 34th Asian Conference on Remote Sensing 2013, ACRS 2013 1, 174–180.

Pinilla Matamala, E., 2011. Informe final. Convenio asesoría integral para la toma de Decisiones en pesca y Acuicultura. Determinación de las condiciones oceanográficas en las áreas Seno de Reloncaví y mar interior de Chiloé. Instituto de Fomento Pesquero.

Potes, M., Costa, M.J., Salgado, R., 2012. Satellite remote sensing of water turbidity in Alqueva reservoir and implications on lake modelling. Hydrol Earth Syst Sci 16, 1623–1633. https://doi.org/10.5194/HESS-16-1623-2012

Preisendorfer, R.W., 1976. Hydrologic Optics, Volumen 1. Introduction. Honululu, Hawaii.

Quang, N.H., Sasaki, J., Higa, H., Huan, N.H., 2017. Spatiotemporal variation of turbidity based on landsat 8 OLI in Cam Ranh Bay and Thuy Trieu Lagoon, Vietnam. Water (Switzerland) 9. https://doi.org/10.3390/W9080570

Rodríguez-Benito, C. V., Navarro, G., Caballero, I., 2020. Using Copernicus Sentinel-2 and Sentinel-3 data to monitor harmful algal blooms in Southern Chile during the COVID-19 lockdown. Mar Pollut Bull 161, 111722. https://doi.org/10.1016/J.MARPOLBUL.2020.111722

Rodríguez-López, L., González-Rodríguez, L., Duran-Llacer, I., García, W., Cardenas, R., Urrutia, R., 2022. Assessment of the Diffuse Attenuation Coefficient of Photosynthetically Active Radiation in a Chilean Lake. Remote Sens (Basel) 14, 4568. https://doi.org/10.3390/RS14184568/S1

Saldías, G.S., Hernández, W., Lara, C., Muñoz, R., Rojas, C., Vásquez, S., Pérez-Santos, I., Soto-Mardones, L., 2021. Seasonal Variability of SST Fronts in the Inner Sea of Chiloé and Its Adjacent Coastal Ocean, Northern Patagonia. Remote Sensing 2021, Vol. 13, Page 181 13, 181. https://doi.org/10.3390/RS13020181

Saldías, G.S., Sobarzo, M., Largier, J., Moffat, C., Letelier, R., 2012. Seasonal variability of turbid river plumes off central Chile based on high-resolution MODIS imagery. Remote Sens Environ 123, 220–233. https://doi.org/10.1016/J.RSE.2012.03.010

Saldías, G.S., Sobarzo, M., Quiñones, R., 2019. Freshwater structure and its seasonal variability off western Patagonia. Prog Oceanogr 174, 143–153. https://doi.org/10.1016/J.POCEAN.2018.10.014

Sandoval, M., Parada, C., Torres, R., 2018. Proposal of an integrated system for forecasting harmful algal blooms (HAB) in Chile. Lat Am J Aquat Res 46, 424–451. https://doi.org/10.3856/VOL46-ISSUE2-FULLTEXT-18

Shen, M., Wang, S., Li, Y., Tang, M., Ma, Y., 2021. Pattern of Turbidity Change in the Middle Reaches of the Yarlung Zangbo River, Southern Tibetan Plateau, from 2007 to 2017. Remote Sensing 2021, Vol. 13, Page 182 13, 182. https://doi.org/10.3390/RS13020182

Smith, V.H., 2003. Eutrophication of freshwater and coastal marine ecosystems: A global problem. Environmental Science and Pollution Research 10, 126–139. https://doi.org/10.1065/ESPR2002.12.142

Snyder, J., Boss, E., Weatherbee, R., Thomas, A.C., Brady, D., Newell, C., 2017. Oyster aquaculture site selection using landsat 8-derived sea surface temperature, turbidity, and chlorophyll a. Front Mar Sci 4, 263366. https://doi.org/10.3389/FMARS.2017.00190/

Soomets, T., Uudeberg, K., Jakovels, D., Brauns, A., Zagars, M., Kutser, T., 2020. Validation and Comparison of Water Quality Products in Baltic Lakes Using Sentinel-2 MSI and Sentinel-3 OLCI Data. Sensors 2020, Vol. 20, Page 742 20, 742. https://doi.org/10.3390/S20030742

Soria, J., Jover, M., Domínguez-Gómez, J.A., 2021. Influence of wind on suspended matter in the water of the albufera of Valencia (Spain). J Mar Sci Eng 9. https://doi.org/10.3390/JMSE9030343

Soriano-González, J., Urrego, E.P., Sòria-Perpinyà, X., Angelats, E., Alcaraz, C., Delegido, J., Ruíz-Verdú, A., Tenjo, C., Vicente, E., Moreno, J., 2022. Towards the Combination of C2RCC Processors for Improving Water Quality Retrieval in Inland and Coastal Areas. Remote Sensing 2022, Vol. 14, Page 1124 14, 1124. https://doi.org/10.3390/RS14051124

Sòria-Perpinyà, X., Delegido, J., Urrego, E.P., Ruíz-Verdú, A., Soria, J.M., Vicente, E., Moreno, J., 2022. Assessment of Sentinel-2-MSI Atmospheric Correction Processors and In Situ Spectrometry Waters Quality Algorithms. Remote Sensing 2022, Vol. 14, Page 4794 14, 4794. https://doi.org/10.3390/RS14194794

Sòria-Perpinyà, X., Vicente, E., Urrego, P., Pereira-Sandoval, M., Tenjo, C., Ruíz-Verdú, A., Delegido, J., Soria, J.M., Peña, R., Moreno, J., 2021. Validation of water quality monitoring algorithms for sentinel-2 and sentinel-3 in mediterranean inland waters with in situ reflectance data. Water (Switzerland) 13. https://doi.org/10.3390/W13050686

Soto, D., León-Muñoz, J., Dresdner, J., Luengo, C., Tapia, F.J., Garreaud, R., 2019. Salmon farming vulnerability to climate change in southern Chile: understanding the biophysical, socioeconomic and governance links. Rev Aquac 11, 354–374. https://doi.org/10.1111/RAQ.12336

Soto-Mardones, L., Letelier, J., Salinas, S., Pinillas, E., Belmar, J.P., 2009. Analysis of oceanographic and atmospheric parameters of Seno Reloncaví. Gayana (Concepc) 73, 141–155.

Subiabre, A., Rojas, C., 1994. Geografía Física de la Región de Los Lagos.

Sun, X., Liu, J., Wang, J., Tian, L., Zhou, Q., Li, J., 2021. Integrated monitoring of lakes' turbidity in Wuhan, China during the COVID-19 epidemic using multi-sensor satellite observations. Int J Digit Earth 14, 443–463. https://doi.org/10.1080/17538947.2020.1868584

Tavora, J., Gonçalves, G.A., Fernandes, E.H., Salama, M.S., van der Wal, D., 2023a. Detecting turbid plumes from satellite remote sensing: State-of-art thresholds and the novel PLUMES algorithm. Front Mar Sci 10. https://doi.org/10.3389/FMARS.2023.1215327

Tavora, J., Jiang, B., Kiffney, T., Bourdin, G., Gray, P.C., de Carvalho, L.S., Hesketh, G., Schild, K.M., de Souza, L.F., Brady, D.C., Boss, E., 2023b. Recipes for the Derivation of Water Quality Parameters Using the High-Spatial-Resolution Data from Sensors on Board Sentinel-2A, Sentinel-2B, Landsat-5, Landsat-7, Landsat-8, and Landsat-9 Satellites. Journal of Remote Sensing (United States) 3. https://doi.org/10.34133/REMOTESENSING.0049/SUPPL_FILE/REMOTESENSING.0049.F1.PDF

Taylor, K.E., 2001. Summarizing multiple aspects of model performance in a single diagram. Journal of Geophysical Research: Atmospheres 106, 7183–7192. https://doi.org/10.1029/2000JD900719

Uudeberg, K., Aavaste, A., Kõks, K.L., Ansper, A., Uusõue, M., Kangro, K., Ansko, I., Ligi, M., Toming, K., Reinart, A., 2020. Opticalwater type guided approach to estimate opticalwater quality parameters. Remote Sens (Basel) 12. https://doi.org/10.3390/RS12060931

Uudeberg, K., Ansko, I., Põru, G., Ansper, A., Reinart, A., 2019. Using opticalwater types to monitor changes in optically complex inland and coastalwaters. Remote Sens (Basel) 11. https://doi.org/10.3390/RS11192297

Valle-Levinson, A., Sarkar, N., Sanay, R., Soto, D., León, J., 2007. Spatial structure of hydrography and flow in a Chilean fjord, Estuario Reloncaví. Estuaries and Coasts 30, 113–126. https://doi.org/10.1007/BF02782972/METRICS

Vanhellemont, Q., 2020. Sensitivity analysis of the dark spectrum fitting atmospheric correction for metre- and decametre-scale satellite imagery using autonomous hyperspectral radiometry. Optics Express, Vol. 28, Issue 20, pp. 29948-29965 28, 29948–29965. https://doi.org/10.1364/OE.397456

Vanhellemont, Q., 2019. Adaptation of the dark spectrum fitting atmospheric correction for aquatic applications of the Landsat and Sentinel-2 archives. Remote Sens Environ 225, 175–192. https://doi.org/10.1016/J.RSE.2019.03.010

Vanhellemont, Q., Ruddick, K., 2021. Atmospheric correction of Sentinel-3/OLCI data for mapping of suspended particulate matter and chlorophyll-a concentration in Belgian turbid coastal waters. Remote Sens Environ 256, 112284. https://doi.org/10.1016/J.RSE.2021.112284

Vanhellemont, Q., Ruddick, K., 2018. Atmospheric correction of metre-scale optical satellite data for inland and coastal water applications. Remote Sens Environ 216, 586–597. https://doi.org/10.1016/J.RSE.2018.07.015

Vanhellemont, Q., Ruddick, K., 2016. ACOLITE FOR SENTINEL-2: AQUATIC APPLICATIONS OF MSI IMAGERY. ESA Special Publication SP 740.

Vanhellemont, Q., Ruddick, K., 2014. Turbid wakes associated with offshore wind turbines observed with Landsat 8. Remote Sens Environ 145, 105–115. https://doi.org/10.1016/J.RSE.2014.01.009

Vantrepotte, V., Loisel, H., Dessailly, D., Mériaux, X., 2012. Optical classification of contrasted coastal waters. Remote Sens Environ 123, 306–323. https://doi.org/10.1016/J.RSE.2012.03.004

Vásquez, S.I., Belén De La Torre, M., Saldías, G.S., Montecinos, A., Lausch, A., Bumberger, J., Oppelt, N., 2021. Meridional Changes in Satellite Chlorophyll and Fluorescence in Optically-Complex Coastal Waters of Northern Patagonia. Remote Sensing 2021, Vol. 13, Page 1026 13, 1026. https://doi.org/10.3390/RS13051026

Vijay Prakash, K., Geetha Vimala, C.S., Preethi Latha, T., Jayaram, C., Nagamani, P. V., Laxmi, C.N.V., 2021. Assessment of Water Quality Along the Southeast Coast of India During COVID-19 Lockdown. Front Mar Sci 8, 338. https://doi.org/10.3389/FMARS.2021.659686/BIBTEX

Werdell, P.J., McKinna, L.I.W., Boss, E., Ackleson, S.G., Craig, S.E., Gregg, W.W., Lee, Z., Maritorena, S., Roesler, C.S., Rousseaux, C.S., Stramski, D., Sullivan, J.M., Twardowski, M.S., Tzortziou, M., Zhang, X., 2018. An overview of approaches and challenges for retrieving marine inherent optical properties from ocean color remote sensing. Prog Oceanogr 160, 186–212. https://doi.org/10.1016/J.POCEAN.2018.01.001

Zhan, Y., Delegido, J., Erena, M., Soria, J.M., Ruiz-Verdú, A., Urrego, P., Sòria-Perpinyà, X., Vicente, E., Moreno, J., 2022. Mar Menor lagoon (SE Spain) chlorophyll-a and turbidity estimation with Sentinel-2. Limnetica 41, 305–323. https://doi.org/10.23818/LIMN.41.18

Zohary, T., Padisák, J., Naselli-Flores, L., 2009. Phytoplankton in the physical environment: beyond nutrients, at the end, there is some light. Hydrobiologia 2009 639:1 639, 261–269. https://doi.org/10.1007/S10750-009-0032-2

ANEXO 1: SUPPLEMENTARY MATERIAL 1

Table 5. SM1 Table 1. Mann-Kendall test statistics

Site	Algorithms	n	M-K Statistic	Standard Error	Z Value	Prob>|Z|	Alpha
R1	Nv09	91	191	291.69	0.65	0.51	0.05
	Nv16	91	191	291.69	0.65	0.51	0.05
R2	Nv09	102	377	345.86	1.09	0.28	0.05
	Nv16	102	377	345.86	1.09	0.28	0.05
R3	Nv09	101	-140	340.81	-0.41	0.68	0.05
	Nv16	101	-142	340.81	-0.41	0.68	0.05
R4	Nv09	103	-271	350.93	-0.77	0.44	0.05
	Nv16	103	-271	350.93	-0.77	0.44	0.05
R5	Nv09	103	-91	350.93	-0.26	0.80	0.05
	Nv16	103	-91	350.93	-0.26	0.80	0.05

Table 6. SM1 Table 2. Temporal serie statistics

Temporal serie								
Site	Algorithm	min (FNU)	max (FNU)	mean (FNU)	median (FNU)	SD	CV(%)	n
R1	Nv09	1.402	27.962	3.725	2.858	3.498	93.9	91
	Nv16	1.808	33.918	4.742	3.673	4.273	90.1	
R2	Nv09	1.161	19.556	2.924	2.453	2.517	86.1	102
	Nv16	1.499	24.176	3.739	3.156	3.115	83.3	
R3	Nv09	0.662	8.721	1.910	1.811	0.992	51.9	101
	Nv16	0.855	11.051	2.458	2.333	1.261	51.3	
R4	Nv09	0.244	5.285	1.426	1.277	0.755	53.0	103
	Nv16	0.316	6.754	1.836	1.647	0.968	52.7	
R5	Nv09	0.090	5.271	1.313	1.134	0.844	64.3	103
	Nv16	0.117	6.735	1.692	1.463	1.082	64.0	

Table 7. SM1 Table 3. Summer statistics

Summer								
Site	Algorithms	min (FNU)	max (FNU)	mean (FNU)	median (FNU)	SD	CV (%)	n
R1	Nv09	2.057	4.997	2.922	2.854	0.710	24.3	20
	Nv16	2.649	6.390	3.753	3.668	0.904	24.1	
R2	Nv09	1.175	3.270	2.074	1.974	0.509	24.5	25
	Nv16	1.516	4.198	2.670	2.543	0.652	24.4	
R3	Nv09	0.662	2.334	1.494	1.478	0.412	27.6	25
	Nv16	0.855	3.002	1.926	1.906	0.529	27.5	
R4	Nv09	0.527	1.721	0.998	1.028	0.293	29.4	27
	Nv16	0.681	2.217	1.288	1.327	0.378	29.3	
R5	Nv09	0.294	1.645	0.894	0.868	0.332	37.2	26
	Nv16	0.380	2.120	1.155	1.120	0.428	37.1	

Table 8. SM1 Table 4. Autumn statistics

Autumn								
Site	Algorithms	min (FNU)	max (FNU)	mean (FNU)	median (FNU)	SD	CV (%)	n
R1	Nv09	1.844	27.962	6.103	3.200	6.597	108.1	21
	Nv16	2.376	33.918	7.664	4.109	8.024	104.7	
R2	Nv09	2.025	19.556	4.836	2.752	4.854	100.4	22
	Nv16	2.608	24.176	6.120	3.538	5.983	97.8	
R3	Nv09	1.566	8.721	2.869	2.439	1.574	54.9	21
	Nv16	2.019	11.051	3.680	3.138	1.990	54.1	
R4	Nv09	0.591	5.285	2.141	2.096	0.960	44.8	24
	Nv16	0.763	6.754	2.754	2.698	1.225	44.5	
R5	Nv09	0.885	5.271	2.262	2.048	0.961	42.5	23
	Nv16	1.143	6.735	2.909	2.637	1.227	42.2	

Table 9. SM1 Table 5. Winter statistics

Winter								
Site	Algorithms	min (FNU)	max (FNU)	mean (FNU)	median (FNU)	SD	CV (%)	n
R1	Nv09	1.402	3.985	2.539	2.448	0.714	28.1	21
	Nv16	1.808	5.108	3.264	3.150	0.912	27.9	
R2	Nv09	1.161	3.372	2.327	2.232	0.571	24.5	20
	Nv16	1.499	4.328	2.993	2.873	0.730	24.4	

R3	Nv09	1.107	3.062	2.006	1.891	0.501	25.0	21
	Nv16	1.428	3.934	2.582	2.436	0.641	24.8	
R4	Nv09	1.038	3.113	1.772	1.716	0.465	26.2	20
	Nv16	1.339	3.997	2.283	2.212	0.596	26.1	
R5	Nv09	0.858	3.316	1.641	1.579	0.572	34.8	20
	Nv16	1.108	4.256	2.113	2.035	0.732	34.7	

Table 10. SM1 Table 6. Spring statistics

Spring								
Site	Algorithms	min (FNU)	max (FNU)	mean (FNU)	median (FNU)	SD	CV (%)	n
R1	Nv09	2.201	7.659	3.416	2.918	1.295	37.9	29
	Nv16	2.833	9.732	4.379	3.750	1.639	37.4	
R2	Nv09	1.313	4.508	2.671	2.534	0.850	31.8	35
	Nv16	1.694	5.771	3.432	3.259	1.085	31.6	
R3	Nv09	0.699	2.892	1.566	1.387	0.599	38.3	34
	Nv16	0.903	3.716	2.017	1.788	0.769	38.1	
R4	Nv09	0.244	2.161	1.033	0.969	0.445	43.1	32
	Nv16	0.316	2.782	1.333	1.251	0.572	42.9	
R5	Nv09	0.090	2.041	0.799	0.781	0.460	57.5	34
	Nv16	0.117	2.629	1.031	1.009	0.592	57.4	

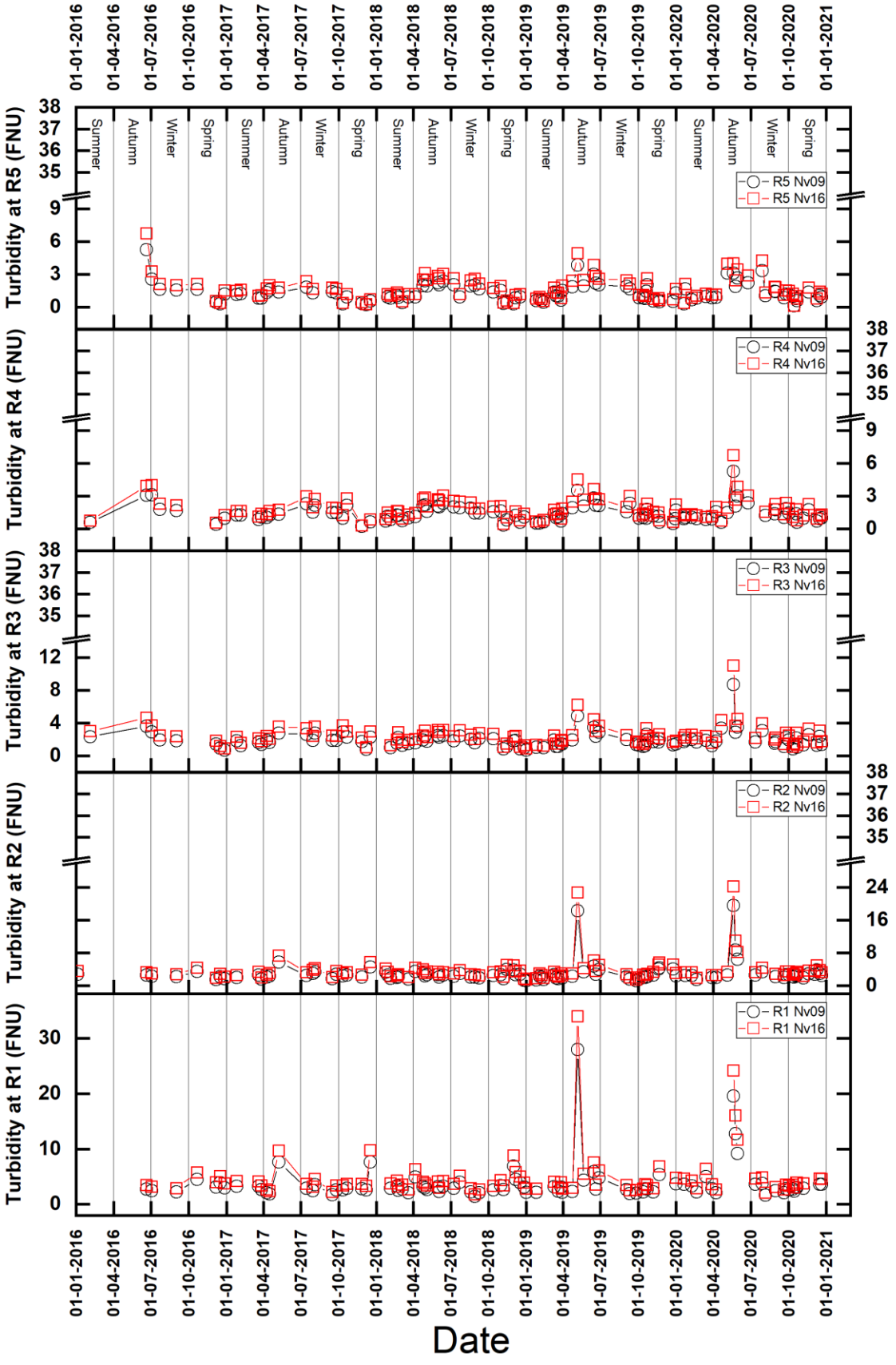
Turbidity at R5 (FNU)
Turbidity at R4 (FNU)
Turbidity at R3 (FNU)
Turbidity at R2 (FNU)
Turbidity at R1 (FNU)
R5 Nv09
R5 Nv16
R4 Nv09
R4 Nv16
R3 Nv09
R3 Nv16
R2 Nv09
R2 Nv16
R1 Nv09
R1 Nv16
Summer
Autumn
Winter
Spring
01-01-2016
01-04-2016
01-07-2016
01-10-2016
01-01-2017
01-04-2017
01-07-2017
01-10-2017
01-01-2018
01-04-2018
01-07-2018
01-10-2018
01-01-2019
01-04-2019
01-07-2019
01-10-2019
01-01-2020
01-04-2020
01-07-2020
01-10-2020
01-01-2021
Date

Figure 8. SM1 Figure 1. Time series of satellite turbidity estimates using both algorithms for the period 2016-2020 in all sites. The black circles and red squares represent the turbidity values from the Nechad 2009 (Nv09) and Nechad 2016 (Nv16) algorithms.

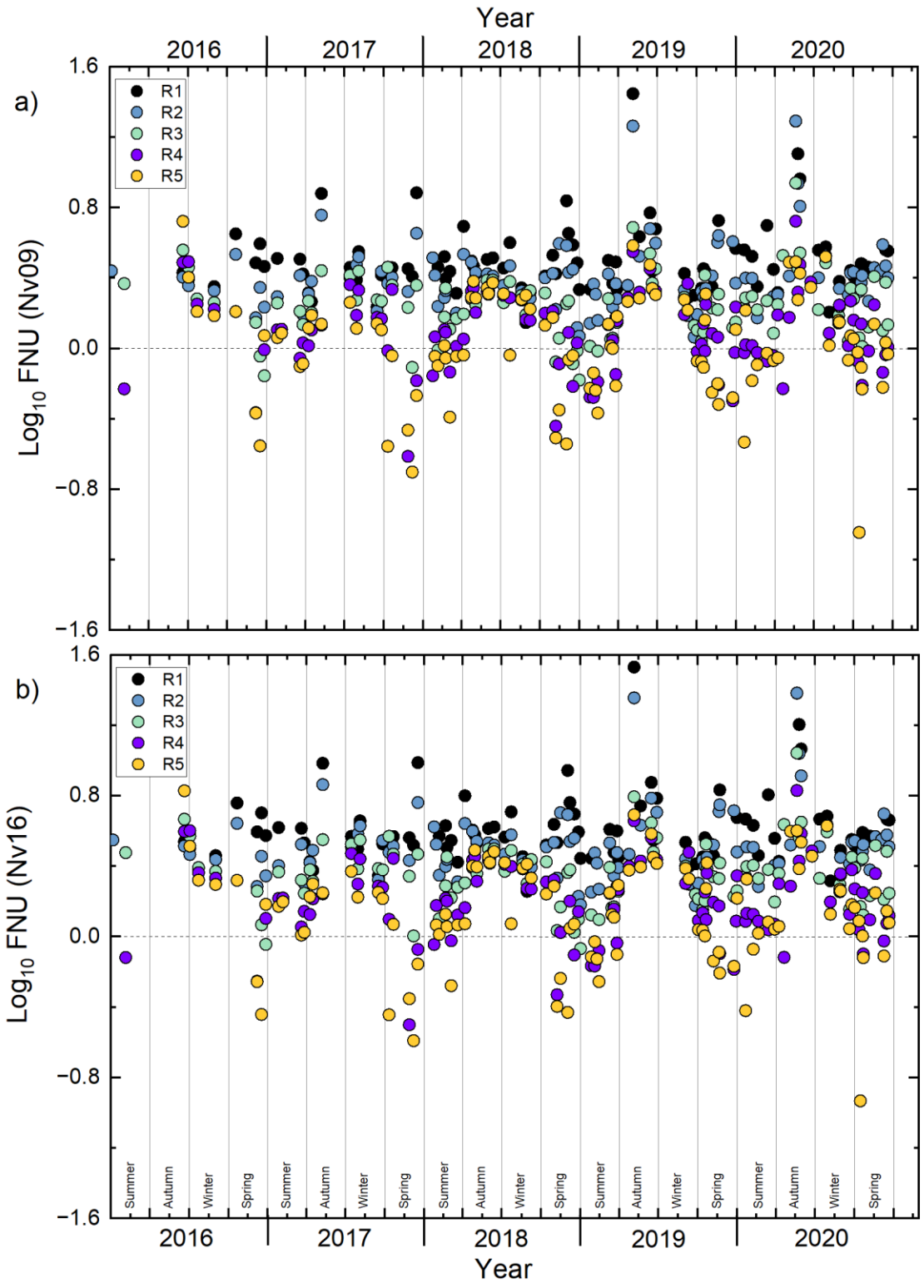

Figura 9. SM1 Figure 2. Spatio-temporal distribution for the five study sites, R1 in black, R2 in light blue, R3 mint, R4 purple and R5 mustard, panel (a) shows data derived from the Nechad 2009 algorithm (Nv09) and (b) data derived from the Nechad 2016 algorithm (Nv16).

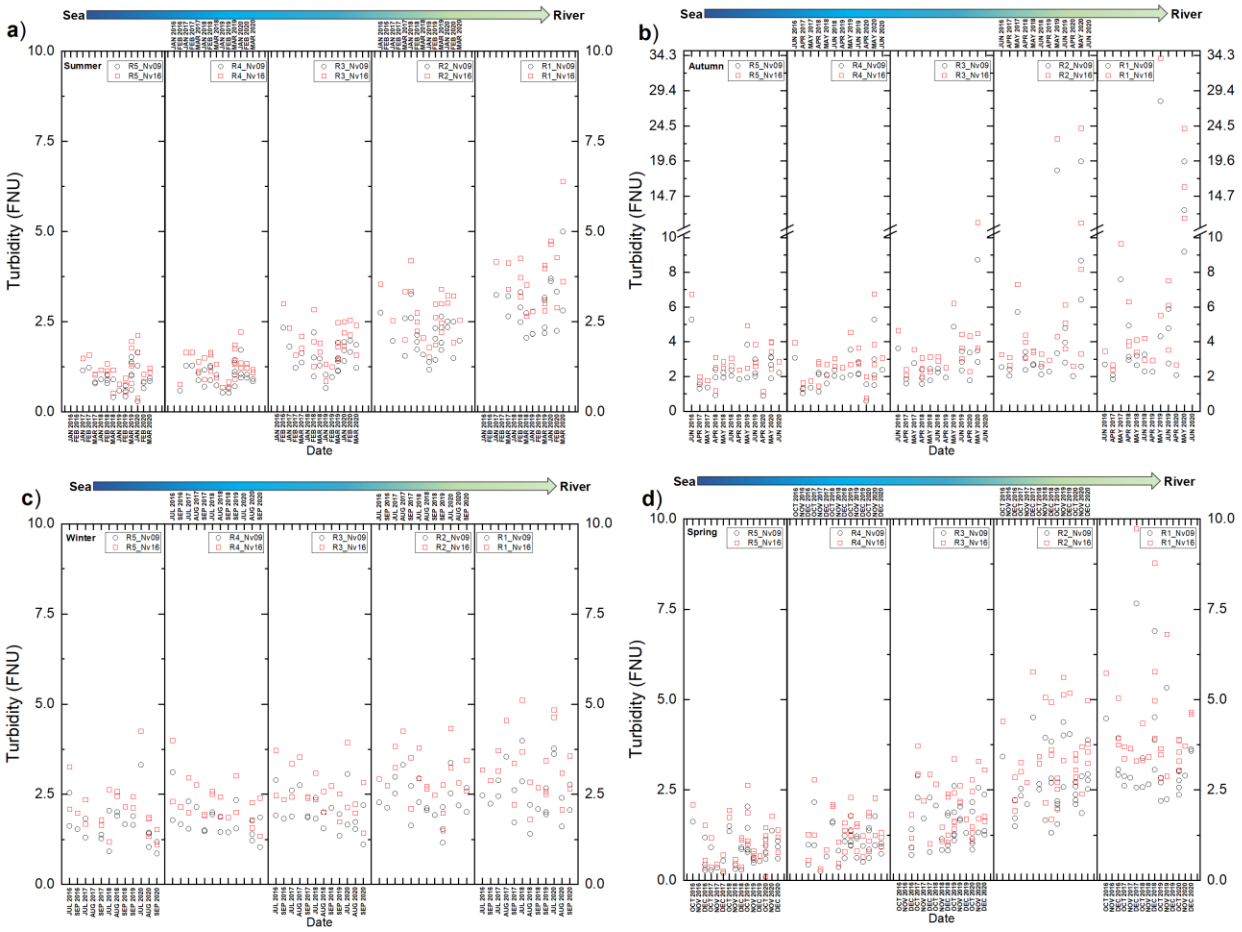

Figure 10. SM1 Figure 3. Seasonal series of turbidity estimated from Nechad 2009 (Nv09, black circles) and Nechad 2016 (Nv16, red squares) algorithms for the five study sites, a) austral summer, b) austral autumn, c) austral winter, d) austral spring.

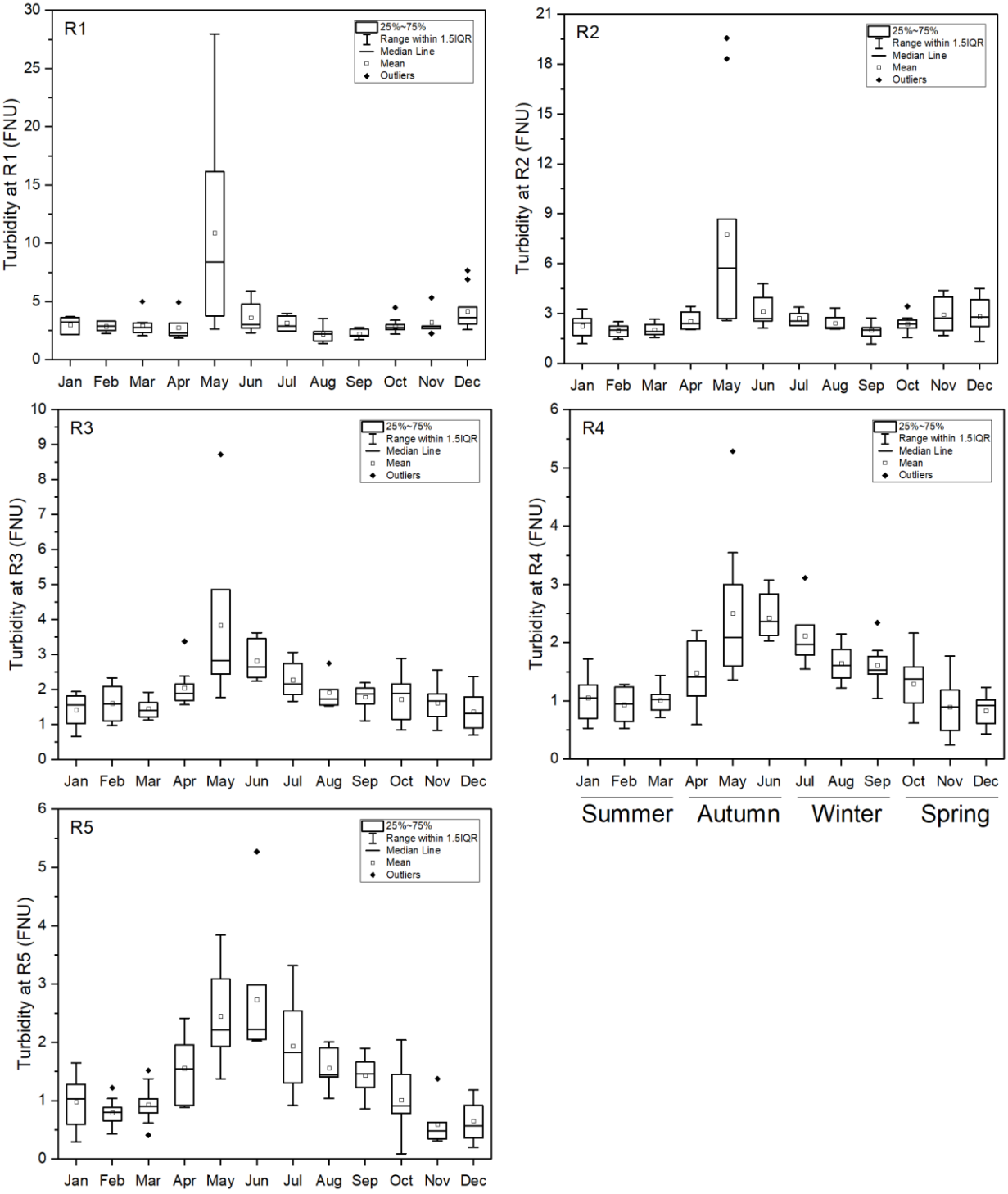

Figura 11. SM1 Figure 4. Monthly boxplot of turbidity time series derived from the Nechad 2009 algorithm (Nv09) for all sites.

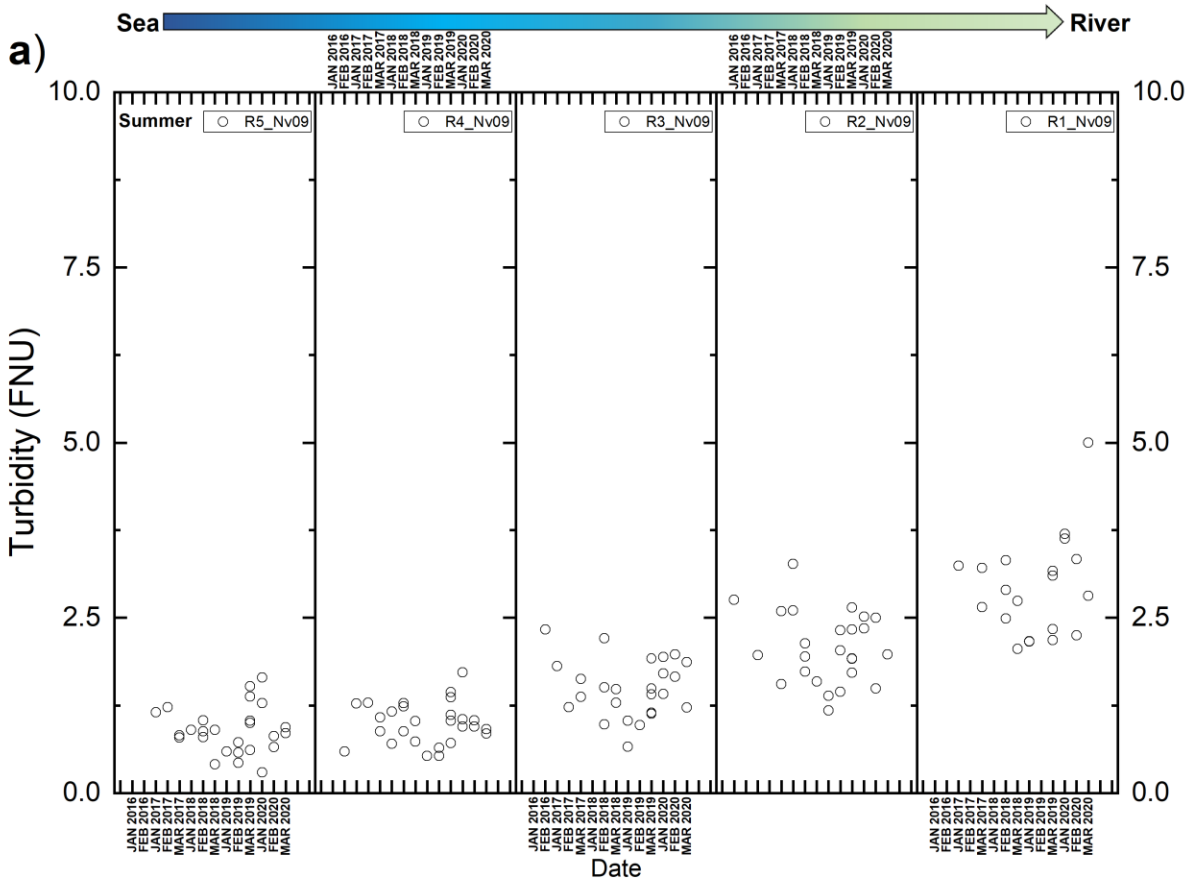

Figure 12. SM1 Figure 5. Seasonal times series of turbidity estimated from Nechad 2009 (Nv09) algorithm for all sites in austral (a) summer, (b) autumn, (c) winter, and (d) spring.

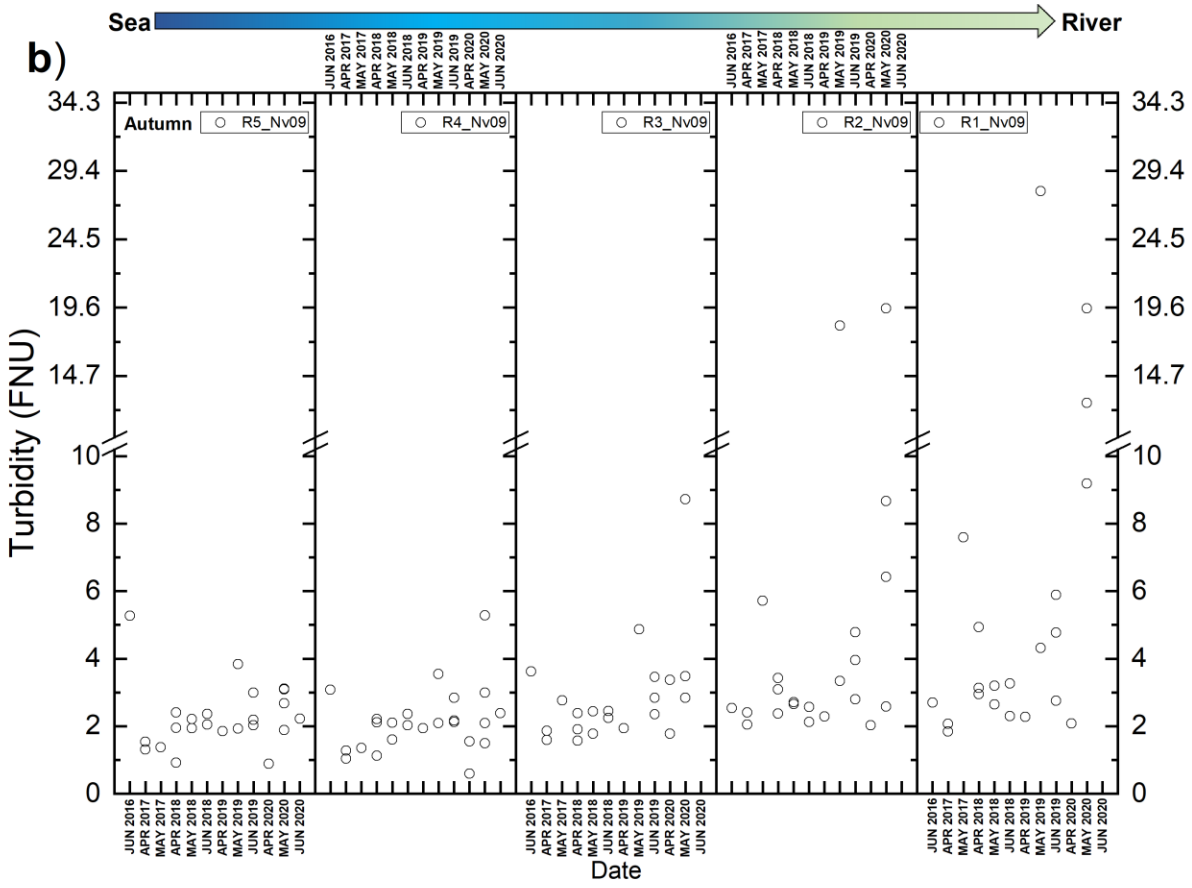

Figure 13. SM1 Figure 5. Seasonal times series of turbidity estimated from Nechad 2009 (Nv09) algorithm for all sites in austral (a) summer, (b) autumn, (c) winter, and (d) spring. Continuation.

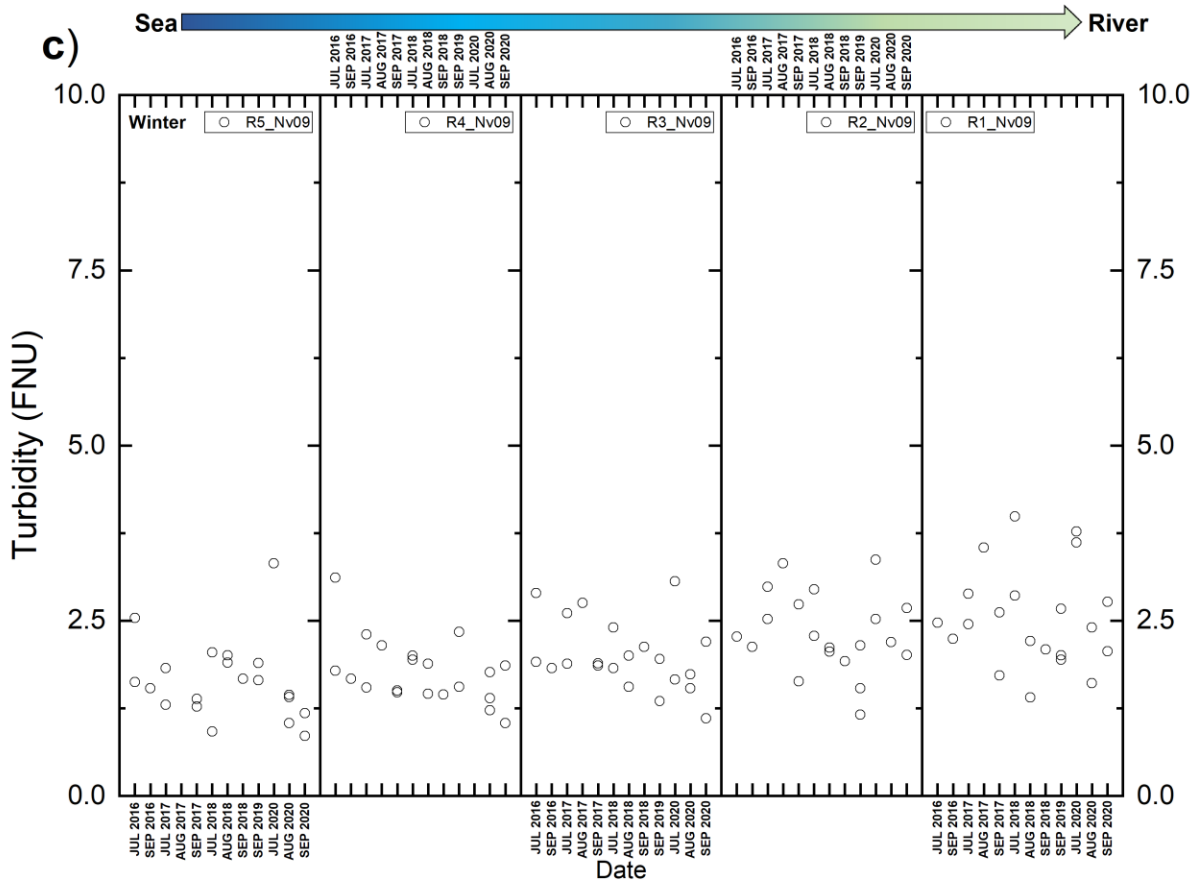

Figure 14. SM1 Figure 5. Seasonal times series of turbidity estimated from Nechad 2009 (Nv09) algorithm for all sites in austral (a) summer, (b) autumn, (c) winter, and (d) spring. Continuation.

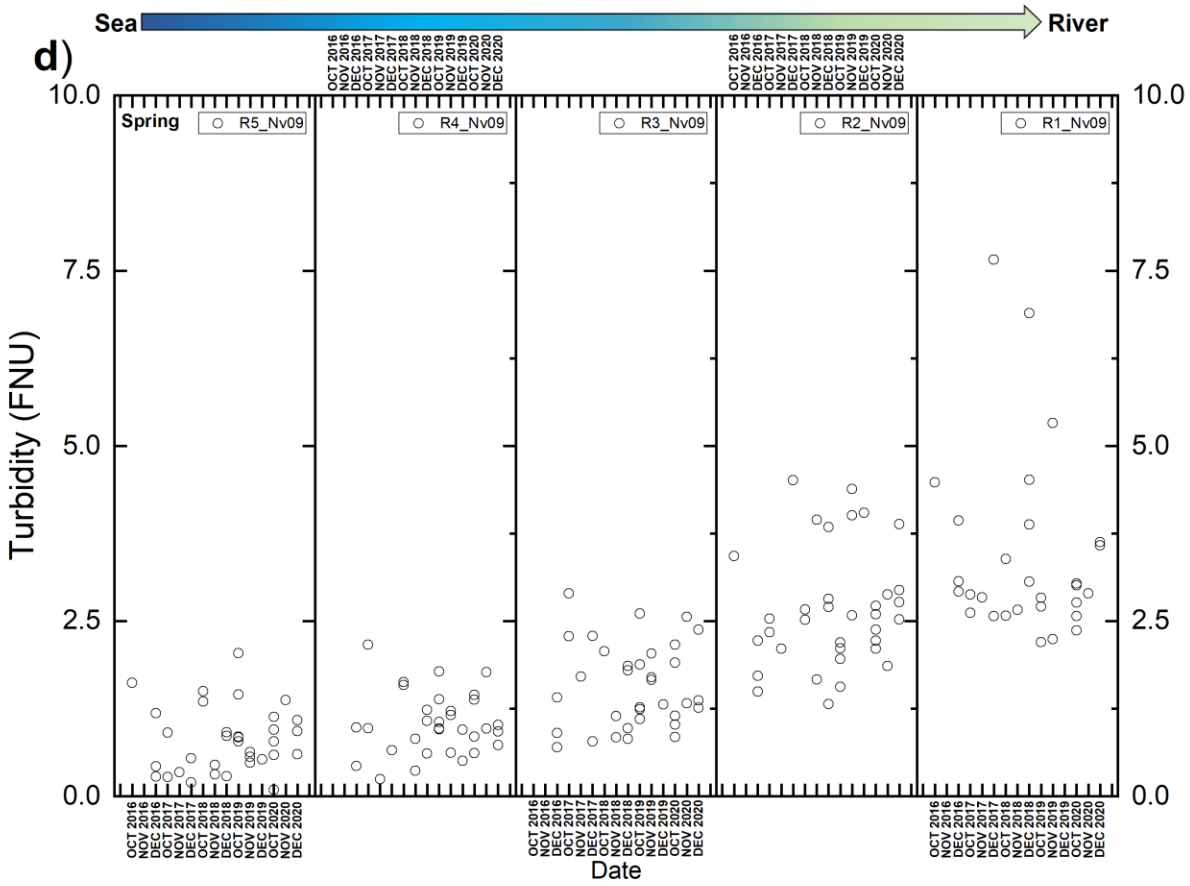

Figure 15. SM1 Figure 5. Seasonal times series of turbidity estimated from Nechad 2009 (Nv09) algorithm for all sites in austral (a) summer, (b) autumn, (c) winter, and (d) spring. Continuation.

ANEXO 2: SUPPLEMENTARY MATTERIAL 2

Table 11. SM2 Table1. Date of acquisition of the images used in this study, their identifier (ID) and percent cloud cover (CC) for the full scene.

Year	Date	Image ID	Cloud cover percentage
2016	05-01-2016	S2A_MSIL1C_20160105T143732_N0201_R096_T18GXU_20160105T145250	0
2016	04-02-2016	S2A_MSIL1C_20160204T143722_N0201_R096_T18GXU_20160204T145334	17.3744
2016	20-06-2016	S2A_MSIL1C_20160620T142752_N0204_R053_T18GXU_20160620T143728	17.0383
2016	03-07-2016	S2A_MSIL1C_20160703T143752_N0204_R096_T18GXU_20160703T144853	0.2001
2016	23-07-2016	S2A_MSIL1C_20160723T143752_N0204_R096_T18GXU_20160723T144933	7.7471
2016	01-09-2016	S2A_MSIL1C_20160901T143752_N0204_R096_T18GXU_20160901T144926	6.8608
2016	21-10-2016	S2A_MSIL1C_20161021T145412_N0204_R096_T18GXU_20161021T145411	6.8587
2016	20-11-2016	S2A_MSIL1C_20161120T145402_N0204_R096_T18GXU_20161120T145401	0.1595
2016	07-12-2016	S2A_MSIL1C_20161207T144402_N0204_R053_T18GXU_20161207T144403	16.8442
2016	17-12-2016	S2A_MSIL1C_20161217T142852_N0204_R053_T18GXU_20161217T144321	8.7217
2016	27-12-2016	S2A_MSIL1C_20161227T142852_N0204_R053_T18GXU_20161227T143749	9.8023
2017	26-01-2017	S2A_MSIL1C_20170126T142851_N0204_R053_T18GXU_20170126T144125	0
2017	05-02-2017	S2A_MSIL1C_20170205T142851_N0204_R053_T18GXU_20170205T144421	5.038
2017	20-03-2017	S2A_MSIL1C_20170320T143741_N0204_R096_T18GXU_20170320T145159	0
2017	27-03-2017	S2A_MSIL1C_20170327T142851_N0204_R053_T18GXU_20170327T143528	4.1432
2017	09-04-2017	S2A_MSIL1C_20170409T143751_N0204_R096_T18GXU_20170409T144933	4.9447
2017	16-04-2017	S2A_MSIL1C_20170416T142751_N0204_R053_T18GXU_20170416T143935	0
2017	09-05-2017	S2A_MSIL1C_20170509T145411_N0205_R096_T18GXU_20170509T145405	0
2017	15-07-2017	S2A_MSIL1C_20170715T144411_N0205_R053_T18GXU_20170715T144411	16.4958
2017	30-07-2017	S2B_MSIL1C_20170730T144409_N0205_R053_T18GXU_20170730T144406	2.2642
2017	04-08-2017	S2A_MSIL1C_20170804T144411_N0205_R053_T18GXU_20170804T144408	31.7417
2017	16-09-2017	S2A_MSIL1C_20170916T143741_N0205_R096_T18GXU_20170916T145118	0.2207
2017	26-09-2017	S2A_MSIL1C_20170926T145401_N0205_R096_T18GXU_20170926T145359	0.0517
2017	11-10-2017	S2B_MSIL1C_20171011T145349_N0205_R096_T18GXU_20171011T145348	1.5473
2017	21-10-2017	S2B_MSIL1C_20171021T143739_N0205_R096_T18GXU_20171021T144945	5.1635
2017	27-11-2017	S2B_MSIL1C_20171127T142739_N0206_R053_T18GXU_20171127T191235	0

2017	07-12-2017	S2B_MSIL1C_20171207T142839_N0206_R053_T18GXU_20171207T174601	11.6566
2017	17-12-2017	S2B_MSIL1C_20171217T142839_N0206_R053_T18GXU_20171217T211305	5.9667
2018	19-01-2018	S2B_MSIL1C_20180119T143749_N0206_R096_T18GXU_20180119T192320	24.8475
2018	24-01-2018	S2A_MSIL1C_20180124T145401_N0206_R096_T18GXU_20180124T161443	0
2018	29-01-2018	S2B_MSIL1C_20180129T143749_N0206_R096_T18GXU_20180129T180250	1.2034
2018	05-02-2018	S2B_MSIL1C_20180205T142849_N0206_R053_T18GXU_20180205T175015	0
2018	20-02-2018	S2A_MSIL1C_20180220T142851_N0206_R053_T18GXU_20180220T205852	1.7402
2018	23-02-2018	S2A_MSIL1C_20180223T143751_N0206_R096_T18GXU_20180223T193944	1.4728
2018	05-03-2018	S2A_MSIL1C_20180305T143751_N0206_R096_T18GXU_20180305T180307	5.5044
2018	20-03-2018	S2B_MSIL1C_20180320T143749_N0206_R096_T18GXU_20180320T193554	10.6073
2018	06-04-2018	S2B_MSIL1C_20180406T142849_N0206_R053_T18GXU_20180406T175248	10.0374
2018	24-04-2018	S2A_MSIL1C_20180424T143751_N0206_R096_T18GXU_20180424T211521	0.0833
2018	29-04-2018	S2B_MSIL1C_20180429T143749_N0206_R096_T18GXU_20180429T193044	8.4425
2018	04-05-2018	S2A_MSIL1C_20180504T143751_N0206_R096_T18GXU_20180504T181252	1.0477
2018	31-05-2018	S2A_MSIL1C_20180531T142901_N0208_R053_T18GXU_20190907T130419	5.848
2018	03-06-2018	S2A_MSIL1C_20180603T143751_N0206_R096_T18GXU_20180603T180407	0
2018	13-06-2018	S2A_MSIL1C_20180613T143751_N0206_R096_T18GXU_20180613T192118	15.1254
2018	08-07-2018	S2B_MSIL1C_20180708T143749_N0206_R096_T18GXU_20180708T193926	9.9732
2018	23-07-2018	S2A_MSIL1C_20180723T143751_N0206_R096_T18GXU_20180723T193740	25.2261
2018	19-08-2018	S2A_MSIL1C_20180819T142751_N0206_R053_T18GXU_20180819T194739	0.2841
2018	29-08-2018	S2A_MSIL1C_20180829T142751_N0206_R053_T18GXU_20180829T194432	4.486
2018	08-09-2018	S2A_MSIL1C_20180908T142751_N0206_R053_T18GXU_20180908T191015	0
2018	13-10-2018	S2B_MSIL1C_20181013T142749_N0206_R053_T18GXU_20181013T193559	9.9725
2018	31-10-2018	S2A_MSIL1C_20181031T143751_N0206_R096_T18GXU_20181103T085637	0.3794
2018	07-11-2018	S2A_MSIL1C_20181107T142751_N0207_R053_T18GXU_20181107T175757	19.7775
2018	15-11-2018	S2B_MSIL1C_20181115T143749_N0207_R096_T18GXU_20181115T182029	27.7134
2018	25-11-2018	S2B_MSIL1C_20181125T143749_N0207_R096_T18GXU_20181125T180007	31.4149
2018	30-11-2018	S2A_MSIL1C_20181130T143741_N0207_R096_T18GXU_20181130T180152	11.3556
2018	02-12-2018	S2B_MSIL1C_20181202T142749_N0207_R053_T18GXU_20181202T175002	0.0105
2018	07-12-2018	S2A_MSIL1C_20181207T142741_N0207_R053_T18GXU_20181207T174902	0
2018	17-12-2018	S2A_MSIL1C_20181217T142741_N0207_R053_T18GXU_20181217T174852	6.6027
2018	27-12-2018	S2A_MSIL1C_20181227T142751_N0207_R053_T18GXU_20181227T174928	28.6669
2019	01-01-2019	S2B_MSIL1C_20190101T142749_N0207_R053_T18GXU_20190101T175051	25.0404

2019	26-01-2019	S2A_MSIL1C_20190126T142751_N0207_R053_T18GXU_20190126T174932	0
2019	03-02-2019	S2B_MSIL1C_20190203T143749_N0207_R096_T18GXU_20190203T193736	0
2019	08-02-2019	S2A_MSIL1C_20190208T143751_N0207_R096_T18GXU_20190208T180253	2.0392
2019	13-02-2019	S2B_MSIL1C_20190213T143749_N0207_R096_T18GXU_20190213T210619	0.3528
2019	10-03-2019	S2A_MSIL1C_20190310T143751_N0207_R096_T18GXU_20190310T180430	0
2019	15-03-2019	S2B_MSIL1C_20190315T143749_N0207_R096_T18GXU_20190315T192124	0.1966
2019	20-03-2019	S2A_MSIL1C_20190320T143751_N0207_R096_T18GXU_20190320T211439	24.316
2019	27-03-2019	S2A_MSIL1C_20190327T142751_N0207_R053_T18GXU_20190327T210145	0
2019	30-03-2019	S2A_MSIL1C_20190330T143751_N0207_R096_T18GXU_20190330T180249	4.5697
2019	24-04-2019	S2B_MSIL1C_20190424T143759_N0207_R096_T18GXU_20190424T192235	1.738
2019	06-05-2019	S2A_MSIL1C_20190506T142801_N0207_R053_T18GXU_20190506T193021	4.2594
2019	21-05-2019	S2B_MSIL1C_20190521T142759_N0207_R053_T18GXU_20190521T175450	16.3495
2019	15-06-2019	S2A_MSIL1C_20190615T142801_N0207_R053_T18GXU_20190615T175159	0.0168
2019	20-06-2019	S2B_MSIL1C_20190620T142759_N0207_R053_T18GXU_20190620T192726	36.9027
2019	28-06-2019	S2A_MSIL1C_20190628T143751_N0207_R096_T18GXU_20190628T193736	2.6118
2019	03-09-2019	S2A_MSIL1C_20190903T142751_N0208_R053_T18GXU_20190903T191006	0.974
2019	11-09-2019	S2B_MSIL1C_20190911T143749_N0208_R096_T18GXU_20190911T193827	52.3697
2019	26-09-2019	S2A_MSIL1C_20190926T143751_N0208_R096_T18GXU_20190926T180247	2.7846
2019	03-10-2019	S2A_MSIL1C_20191003T142801_N0208_R053_T18GXU_20191003T175237	1.1515
2019	13-10-2019	S2A_MSIL1C_20191013T142731_N0208_R053_T18GXU_20191013T174904	0
2019	18-10-2019	S2B_MSIL1C_20191018T142759_N0208_R053_T18GXU_20191018T175428	11.9128
2019	21-10-2019	S2B_MSIL1C_20191021T143749_N0208_R096_T18GXU_20191021T180036	15.7237
2019	23-10-2019	S2A_MSIL1C_20191023T142731_N0208_R053_T18GXU_20191023T175243	6.3915
2019	07-11-2019	S2B_MSIL1C_20191107T142729_N0208_R053_T18GXU_20191107T175146	6.606
2019	20-11-2019	S2B_MSIL1C_20191120T143729_N0208_R096_T18GXU_20191120T180001	10.0114
2019	22-11-2019	S2A_MSIL1C_20191122T142731_N0208_R053_T18GXU_20191122T174913	0.3882
2019	22-12-2019	S2A_MSIL1C_20191222T142731_N0208_R053_T18GXU_20191222T174743	45.7815
2019	25-12-2019	S2A_MSIL1C_20191225T143721_N0208_R096_T18GXU_20191225T175839	51.6761
2019	30-12-2019	S2B_MSIL1C_20191230T143719_N0208_R096_T18GXU_20191230T175959	23.2764
2020	01-01-2020	S2A_MSIL1C_20200101T142731_N0208_R053_T18GXU_20200101T174749	0.7537
2020	04-01-2020	S2A_MSIL1C_20200104T143721_N0208_R096_T18GXU_20200104T175849	27.1669
2020	11-01-2020	S2A_MSIL1C_20200111T142701_N0208_R053_T18GXU_20200111T174818	37.2933
2020	16-01-2020	S2B_MSIL1C_20200116T142649_N0208_R053_T18GXU_20200116T175019	0.2162

2020	21-01-2020	S2A_MSIL1C_20200121T142651_N0208_R053_T18GXU_20200121T175014	3.9313
2020	24-01-2020	S2A_MSIL1C_20200124T143651_N0208_R096_T18GXU_20200124T175925	27.8511
2020	08-02-2020	S2B_MSIL1C_20200208T143659_N0209_R096_T18GXU_20200208T180031	0.0053
2020	20-02-2020	S2A_MSIL1C_20200220T142651_N0209_R053_T18GXU_20200220T175302	0
2020	14-03-2020	S2A_MSIL1C_20200314T143721_N0209_R096_T18GXU_20200314T180039	16.9505
2020	29-03-2020	S2B_MSIL1C_20200329T143729_N0209_R096_T18GXU_20200329T193330	4.7419
2020	08-04-2020	S2B_MSIL1C_20200408T143729_N0209_R096_T18GXU_20200408T193410	0
2020	20-04-2020	S2A_MSIL1C_20200420T142731_N0209_R053_T18GXU_20200420T175257	5.9281
2020	05-05-2020	S2B_MSIL1C_20200505T142729_N0209_R053_T18GXU_20200505T174917	57.907
2020	20-05-2020	S2A_MSIL1C_20200520T142741_N0209_R053_T18GXU_20200520T175228	9.5782
2020	25-05-2020	S2B_MSIL1C_20200525T142729_N0209_R053_T18GXU_20200525T174759	10.7745
2020	30-05-2020	S2A_MSIL1C_20200530T142741_N0209_R053_T18GXU_20200530T175048	1.8223
2020	24-06-2020	S2B_MSIL1C_20200624T142739_N0209_R053_T18GXU_20200624T174931	29.5346
2020	12-07-2020	S2A_MSIL1C_20200712T143731_N0209_R096_T18GXU_20200712T192236	10.64
2020	29-07-2020	S2A_MSIL1C_20200729T142741_N0209_R053_T18GXU_20200729T180053	2.2197
2020	06-08-2020	S2B_MSIL1C_20200806T143729_N0209_R096_T18GXU_20200806T180908	40.2235
2020	28-08-2020	S2A_MSIL1C_20200828T142741_N0209_R053_T18GXU_20200828T175951	15.5935
2020	30-08-2020	S2A_MSIL1C_20200831T143731_N0209_R096_T18GXU_20200831T194902	8.4296
2020	20-09-2020	S2A_MSIL1C_20200920T143731_N0209_R096_T18GXU_20200920T194735	0.7446
2020	25-09-2020	S2B_MSIL1C_20200925T143729_N0209_R096_T18GXU_20200925T182726	0.1081
2020	02-10-2020	S2B_MSIL1C_20201002T142739_N0209_R053_T18GXU_20201002T175850	41.3463
2020	12-10-2020	S2B_MSIL1C_20201012T142739_N0209_R053_T18GXU_20201012T175341	9.6773
2020	15-10-2020	S2B_MSIL1C_20201015T143729_N0209_R096_T18GXU_20201015T181134	0.0013
2020	20-10-2020	S2A_MSIL1C_20201020T143731_N0209_R096_T18GXU_20201020T181238	0.4462
2020	22-10-2020	S2B_MSIL1C_20201022T142739_N0209_R053_T18GXU_20201022T180110	0
2020	06-11-2020	S2A_MSIL1C_20201106T142741_N0209_R053_T18GXU_20201106T181041	7.313
2020	19-11-2020	S2A_MSIL1C_20201119T143731_N0209_R096_T18GXU_20201119T181130	3.5595
2020	04-12-2020	S2B_MSIL1C_20201204T143729_N0209_R096_T18GXU_20201204T180911	0.0777
2020	09-12-2020	S2A_MSIL1C_20201209T143721_N0209_R096_T18GXU_20201209T181054	28.6217
2020	16-12-2020	S2A_MSIL1C_20201216T142731_N0209_R053_T18GXU_20201216T175850	6.109
2020	21-12-2020	S2B_MSIL1C_20201221T142729_N0209_R053_T18GXU_20201221T175831	1.3954